

# Automatic Segmentation of the Mouse Skull in MR Images for MRI Guided Focused Ultrasound Therapy

Bachelor Thesis

of

## Luca Springer

At the KIT Department of Informatics  
Institute for Anthropomatics and Robotics (IAR) -  
Health Robotics and Automation (HERA)

and the

Institute for Data Processing and Electronics (IPE)

First reviewer: Prof. Dr. Franziska Mathis-Ullrich  
Second reviewer: Dr. Torsten Hopp  
Advisor: M. Sc. Paul Scheikl

04. January 2021 – 03. May 2021

# Abstract

## Automatic Segmentation of the Mouse Skull in MR Images for MRI Guided Focused Ultrasound Therapy

MRI-guided Focused Ultrasound is used to open the blood-brain barrier of mice. Sonication simulations aid the individual optimization of the sonication parameters for each mouse. For the automation of this process, automatic segmentation of the mouse skull in pre-sonication MR scans is necessary.

The segmentation of the mouse skull in MR images is challenging because bone tissue has a low signal in MRI. There is neither enough labeled data to train a neural network for this challenge nor any literature proposing a method for the automatic segmentation of the mouse skull in MR images. This thesis suggests, implements, and evaluates an approach for automatic skull segmentation of the mouse skull in MR images.

The slice-based approach uses well-established methods of medical image processing. The skull segmentation uses empirical knowledge about the anatomy of the mouse head to combine the result of a brain segmentation and a foreground segmentation. The foreground segmentation uses morphological operations and adaptive binarization to identify dark structures of the mouse head. The brain segmentation makes use of the fully automatic 3D-PCNN algorithm and improves the result by incorporating an additional bias field correction beforehand. Post-processing improves the skull segmentation by closing small gaps between two skull segments.

In this thesis, the segmentation result for four different MRI sequences is evaluated using Dice score and Matthews Correlation Coefficient. For most MRI sequences, the median of both scores for the skullcap is approximately 0.8 and 0.7 for the whole image, respectively. Additionally, the brain is segmented for acoustic simulations with a median score of approximately 0.85.

The implementation of the approach can be used in the future to optimize the MRI-guided FUS system parameters automatically. The suggested approach enables the automatic optimization of the sonication parameters without the requirement for additional adjustments of the blood-brain barrier opening protocol. Consequently, this thesis is an important part of a joint project of the KIT and the University of Heidelberg. The project aims to enable a robust blood-brain barrier opening in mice for stem cell application. The approach developed in this thesis can be used as a comparison for further suggestions in the future.

**Keywords:** *automatic segmentation, mouse, rodent, skull, brain, MRI, FUS, MRgFUS*

# Contents

<b>Abstract</b>	<b>vii</b>
<b>Zusammenfassung</b>	<b>ix</b>
<b>1. Introduction</b>	<b>1</b>
1.1. Challenges . . . . .	1
1.2. Research goal . . . . .	3
<b>2. State of the art</b>	<b>5</b>
<b>3. Methods</b>	<b>7</b>
3.1. Prior observations . . . . .	7
3.2. Read data . . . . .	9
3.3. Pre-processing . . . . .	10
3.3.1. Histogram equalization . . . . .	10
3.3.2. Contrast enhancement . . . . .	11
3.3.3. Image denoising . . . . .	11
3.4. Segmentation . . . . .	13
3.4.1. Foreground segmentation . . . . .	13
3.4.2. Brain segmentation . . . . .	15
3.4.2.1. Bias field correction . . . . .	15
3.4.2.2. 3D-PCNN segmentation . . . . .	16
3.4.2.3. Post-processing of the brain segmentation . . . . .	18
3.4.3. Skull segmentation . . . . .	19
3.5. Post-processing . . . . .	22
<b>4. Results</b>	<b>25</b>
4.1. Metrics . . . . .	25
4.1.1. Dice score . . . . .	25
4.1.2. Matthews Correlation Coefficient . . . . .	26
4.2. Optimization of the brain segmentation . . . . .	26
4.3. Optimization of the foreground segmentation . . . . .	31
4.4. Evaluation of the entire automatic segmentation . . . . .	35
4.5. Performance . . . . .	38
<b>5. Summary, Discussion and Conclusion</b>	<b>41</b>
<b>Bibliography</b>	<b>43</b>
<b>Appendix</b>	<b>47</b>
A. Algorithms . . . . .	47
B. Additional Figures . . . . .	48

<b>Glossary</b>	<b>59</b>
<b>Acronyms</b>	<b>61</b>
<b>List of Figures</b>	<b>64</b>
<b>List of Tables</b>	<b>65</b>
<b>List of Algorithms</b>	<b>67</b>

# 1. Introduction

Alzheimer's disease (AD) is the most common cause of dementia in the western world. The number of AD cases will most likely grow until 2050, before the increase levels off. In 2020, an estimated 5.8 million Americans age 65 and older suffered from AD. This number could increase to 13.8 million by 2050 [2, 1].

Possible regenerative therapy for neurodegenerative disorders like AD is the treatment with stem cells, but their application to the brain parenchyma requires an opening of the blood-brain barrier (BBB). Focused Ultrasound (FUS) enables non-invasive, local, and transient BBB opening. The combination with Magnetic Resonance Imaging (MRI) allows guidance, targeting, and monitoring in real-time (MRgFUS). A HEiKA project involving the Medical Faculty Mannheim in collaboration with the Institute for Data Processing and Electronics (IPE) at Karlsruhe Institute of Technology (KIT) aims to develop a reliable BBB opening protocol in mice using MRgFUS. This thesis is part of that project [32].

Because of the reflective and attenuating properties of skull bone tissue, the sonication has to be optimized for each mouse individually. Pre-opening MRI scans of the mouse skull before the actual sonication provide MRI sequences that should be used to generate data for acoustic simulations using a model of the individual skull. For this purpose, the skull contained in an MRI sequence must be segmented. Cardenas et al. [5] state that automatic segmentation methods address challenges like "inter- and intraobserver variability," which occur in (partly) manual segmentation processes. Additionally, using an automatic segmentation method enables the automation of FUS parameter optimization in our project.

## 1.1. Challenges

There are several challenges when processing bone tissue in Magnetic Resonance (MR) slices. Bone tissue features a low signal in MR slices. Therefore, the bone tissue shows common gray values similar to the background, and the signal-to-noise ratio (SNR) is worse in conventional MRI sequences such as T1 weighted or T2 weighted images. Additionally, the mouse skull is thin with a thickness between 0.1 and 0.7 mm [15]. Even though typical MRI resolutions in small animal research are 0.1 – 0.025 mm [20], this results in a skull thickness of only a few pixels. The duration of the pre-sonication scans is kept low, which manifests in a low amount of slices, large slice thickness, and ample spacing between slices (see also figure 1.3).

Each slice resides in the transversal plane and is isometric. However, when using 3D segmentation methods and interpreting the sequence as volume, its non-isometric property must be considered. Also, because of the large slice thickness and the curvature of the brain surface, it is more likely that multiple types of tissue occur in one pixel. This effect

## 1. Introduction

---

leads to partial volume effect (PVE) artifacts [23]. Figure 1.1 depicts an exemplary pre-opening scan. The dynamic range is extensive in the data set. Therefore, the contrast is relatively low with linear scaling.

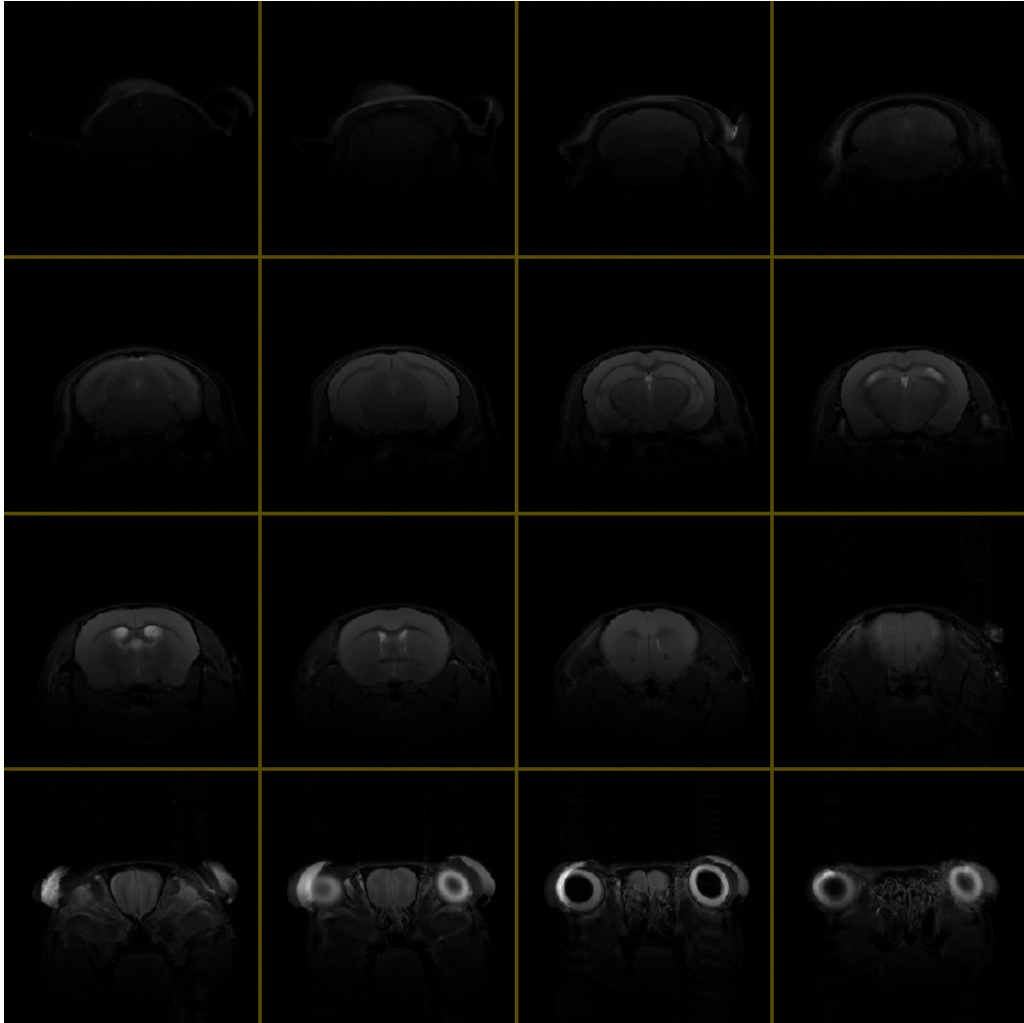


**Figure 1.1.:** Representation of sequence 03 (table 3.1), T2 weighted.  
Top to bottom: Slices 1-4 (at Lambda), 5-8, 9-12, 13-16 (between the eyes).

Sequences provided by the pre-opening scans do not depict the whole skull, as the brain is the region of interest for FUS. The red area depicted in figure 1.2 also gives a rough impression of the location of the slices. The sonication is applied in the dorsal direction, which means the skullcap is of greater interest to the simulation than other parts of the skull, i.e., the mandible. Because the slices lie in the transverse plane, the thickness of the skullcap is well represented in each slice.

Several automatic segmentation methods for cranial human MRI scans exist [37, 10, 40, 25]. However, no literature suggesting an approach for automatic segmentation of the skull in rodent cranial scans has been presented.

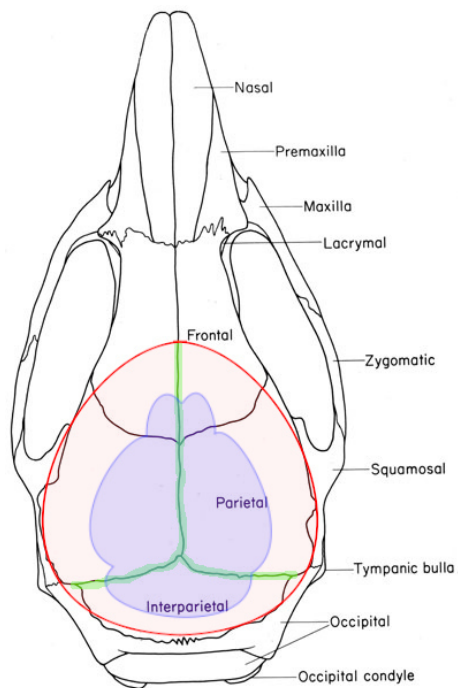


**Figure 1.2.:** Dorsal skull aspect as shown in Cook [8]. Red: Region of interest. Green: Thicker parts of the skull. Blue: Approximate location of the brain.

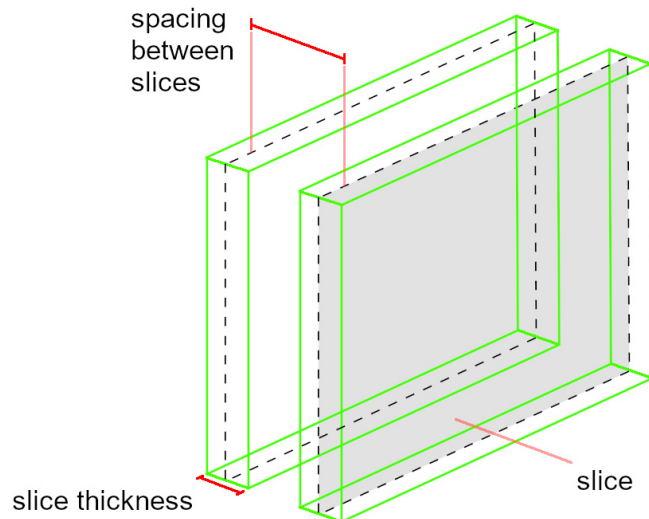


**Figure 1.3.:** Slice thickness and spacing between slices.

## 1.2. Research goal

This thesis addresses this shortcoming. An approach for automatic segmentation of the mouse skull in conventional T2 weighted MR slices should be developed concerning the mentioned challenges (figure 1.4), enabling automated subject-specific optimization of FUS parameters. The suggested approach should be implemented with MATLAB 2020b. It has to be capable of being used within the framework of the HEiKA project without

## 1. Introduction

---

any further adjustment of the MRI protocol. Finally, the method should be analyzed with respect to its quality.

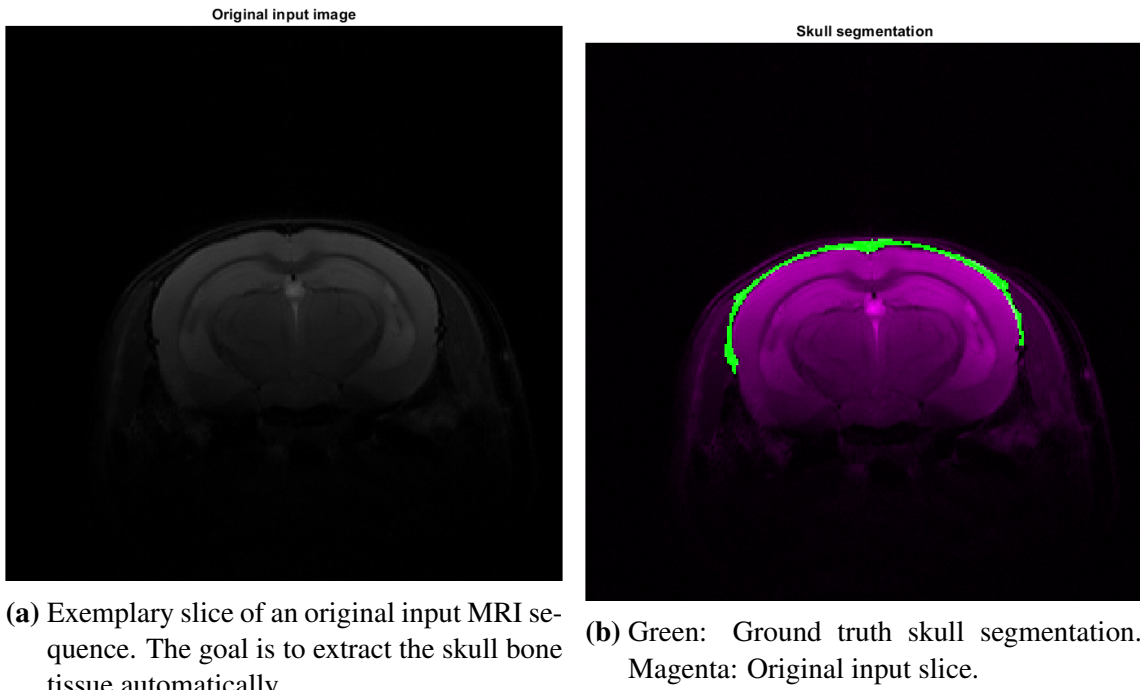


**Figure 1.4.:** Depiction of an optimal skull segmentation.

## 2. State of the art

In order to develop an approach to the problem described in chapter 1, it is helpful to take a step back and get an overview of segmentation methods in general. This chapter collects and discusses current approaches in the field of medical image segmentation.

In image processing, the segmentation of an image can be interpreted as the extraction of certain information, which may differ depending on the task. This process primarily includes pre-processing the image to correct imaging errors or highlight certain aspects. Segmenting an image involves many features: Pixel-based properties like intensity can be used to segment an image with thresholding. Thresholding assigns pixels to one of many classes based on their gray value. Furthermore, environment-based properties like the shape, location, or texture of the objects provide additional information. Edge-based algorithms detect the edges in an image with the use of pixel value gradients or difference operators. Morphological operations can correct segmentation artifacts, fill holes in a segment or remove the background. In image sequences, time-based properties aid in establishing further relations between the objects in multiple images [26].

Besides the traditional methods, many advanced approaches to image segmentation were proposed. Ding et al. [10] use the level set method to track the skull shape in human MRI to segment the skull automatically. Also, statistical shape information from human Computed Tomography (CT) data was used for the same purpose [37].

With the advance in computational power and the ability to perform well-defined tasks consistently and continuously, machine learning algorithms gained popularity over the last two decades (see figure B.1). In the medical field, these algorithms are used for computer-aided diagnosis and in decision support systems. Furthermore, patterns invisible to the human eye can be recognized. The parallel computing power of modern graphic processing units enables neural network architectures with more than 20 layers, also known as deep learning. Well-known neural networks in medical fields like radiology are Convolutional Neural Networks (CNNs), which have been applied in several image classification tasks. During the training phase, these networks require large data sets. Pre-trained CNNs can be used to solve tasks that are different from tasks they were trained for. This approach is called transfer learning [13, 16]. Many methods presented at the conference on image processing in medicine in 2020 suggest deep learning approaches [36]. Automatic approaches for segmentation are used and developed increasingly to spare time and avoid “interindividual variability between the evaluators” [12] of partly manual or completely manual segmentation approaches.

MR images, due to the strong soft tissue contrast of MRI, are suitable for the segmentation of the brain or other parts of an organism with a high proportion of water or fat. Nevertheless, the bone tissue is more distinctive in CT images than in MR images. Figure 2.1 shows that that fewer papers are dealing with automatic segmentation of bone tissue in MR images than in CT images.

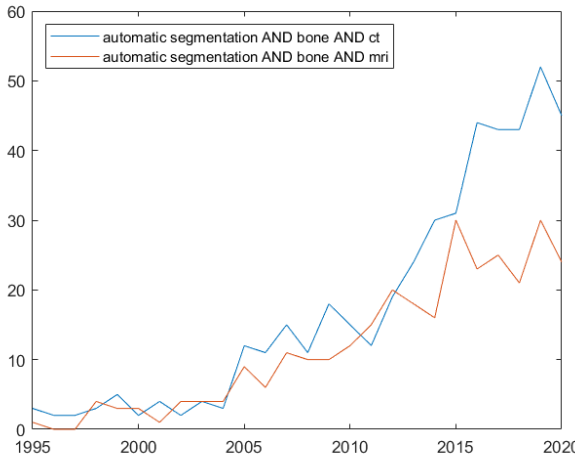


**Figure 2.1.:** Number of papers in PubMed<sup>1</sup> for searches on automatic segmentation of bone in CT (respective MR) images from 1995 to 2020 (linear vertical scale).

Because the image segmentation in MRI is limited chiefly to soft tissue, many papers propose algorithms for automatic segmentation of brain tissue in rodent MRI scans [7, 27, 17, 19]. Feo and Giove [14] critically review several methods for the segmentation of rodent brains in MR images. They mainly focus on T2 weighted volumes due to the better contrast for small rodents. Correcting the bias field before skull-stripping and segmenting the volumes can improve the result of automatic segmentation methods. The Three-dimensional Pulse-coupled Neural Network Algorithm (3D-PCNN) is a feasible approach to segment the rodent brain. However, a fully convolutional approach implemented by Guha Roy et al. [17] can segment the rodent brain in MRI volumes with an isometric resolution of  $256 \times 256 \times 256$  px in 20 seconds (deployed on Titan X Pascal 12GB GPU in Linux Ubuntu 16.04 OS)<sup>2</sup>. This implementation is based on U-Net and uses the computational power of graphic processing units. Tidwell et al. [34] use MRI and Diffusion-weighted Imaging (DWI) to segment the rodent spinal cord in MR images automatically. Instead of implementing a contour-based segmentation approach, the Classification Expectation Maximization (CEM) algorithm is used. The intensity values of a T2 weighted MR image are interpreted as a sum of intensity values from the background as well as the cord and cerebrospinal fluid. The respective intensity values follow a Gaussian distribution.

Several approaches exist for segmenting the human skull in MRI images. Tools like FSL BET2[29] and BrainSuite[11] can extract inner and outer skull surfaces in cranial human MR images [25]. Morphological operations applied to T1 weighted and T2 weighted images can improve the segmentation results. Because the anatomy of the mouse head and the human head differ significantly, these approaches can not be applied directly to our problem.

Segmenting rodent bone structures is challenging. Wiens [39] presents an approach to automatically segment complex bone structures of rodents in Micro-computed Tomography ( $\mu$ CT) scans using a Reeb graph. To our knowledge, there is no literature focusing on segmenting the rodent skull in MRI images automatically.

<sup>1</sup>Data acquired from <https://pubmed.ncbi.nlm.nih.gov/>, accessed 2021-04-10.

<sup>2</sup><https://github.com/ai-med/QuickNATv2>, accessed 2021-04-12.

# 3. Methods

This chapter presents the general approach to segment the mouse skull in rodent MR images automatically. The method developed in this work will be referred to as Automatic Segmentation of the Mouse Skull in MR images (AuSoMS). AuSoMS uses methods chosen based on the boundaries of the HEiKA project depicted in section 3.1. Additionally, the implementation incorporates the findings in chapter 2, and observations during the development process of AuSoMS.

## 3.1. Prior observations

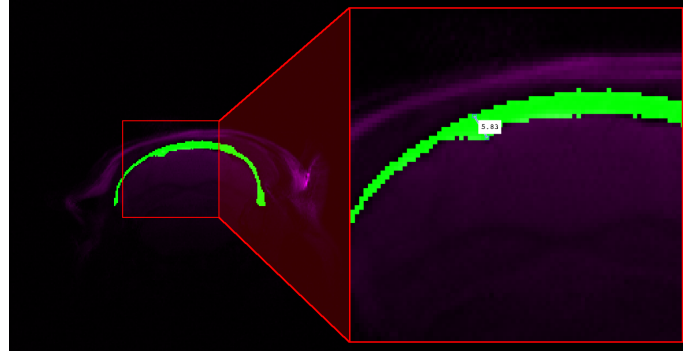
As a starting point the data sets, which were available during this work, are listed. Based on the situation at hand, requirements are placed on the automatic segmentation of the available data.

Four different MRI sequences in the DICOM standard are available (table 3.1). The images were acquired *in vivo* with the preclinical MRI scanner *BioSpec 94/20 AVII (Bruker Inc.)* in cranial direction (transverse plane). Each sequence is available with T2 weighted imaging settings. AuSoMS focuses on T2 weighted sequences because T1 weighted sequences show less contrast between bone tissue and surrounding soft tissue [14].

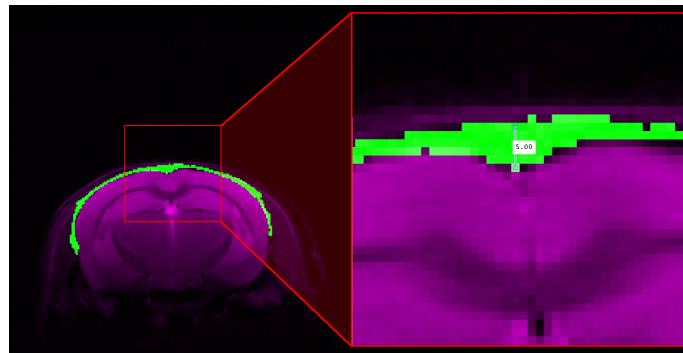
**Table 3.1.: DICOM sequences**

ID	Number of slices	Slice size [px]	Pixel spacing [mm]	Slice thickness [mm]	Spacing between slices [mm]
03	16	256 × 256	0.0781 × 0.0781	0.8	1
04	16	256 × 256	0.0781 × 0.0781	0.8	1
ZI	29	256 × 256	0.0781 × 0.0781	0.4	0.5
ME	12	512 × 512	0.0431 × 0.0431	0.5	1

Assuming the skull thickness is between 0.1 and 0.7 mm [15] - and looking at the pixel dimensions in table 3.1 - the anticipated thickness of the skull in each original slice is in the range of [1, 9] px in sequences *03*, *04*, *ZI* and [2, 17] px in sequence *ME*. Figure 3.1 shows two samples for the thickness of the skullcap measured by hand using ground truth data. The non-isometric sequences are stored as a stack of slices (e.g., sequence *03*: 256 × 256 × 16). Instead of interpolating the slices to transform the sequence into an isometric volume, the automatic segmentation is slice-based.



**(a)** Spot check of thickness in a slice located approximately at the Lambda. Measured thickness is 5.83 pixels ( $\approx 0.453$  mm).



**(b)** Spot check of thickness in a slice depicting a transversal excerpt of the parietal bone. Measured thickness is 5 pixels ( $\approx 0.390$  mm).

**Figure 3.1.:** Approximated skull thickness in exemplary slices of sequence 03 using ground truth data. Original slice is colored magenta. Ground truth is colored green. The distances are measured by hand.

A rater involved in the HEiKA project provides the ground truth of all data sets. The rater labeled both brain and bone tissue in each slice of the original MRI sequences manually using the available tools of the Medical Imaging Interaction Toolkit (MITK). The most important part of the skull is the skullcap since the geometry of the segmentation result is used for the FUS simulation. The influence of reflections or attenuation of the ultrasound wave occurring at the other parts of the skull has a negligible effect on the focal point of the FUS. Therefore, the segmentation of these areas is assigned a lower priority level than the segmentation of the skullcap.

Figure B.4 depicts the ground truth of sequence 03. A specific gray value profile of the skull segments can be identified. However, the histograms seem to cover a broad spectrum of grayscale values. The width of the spectrum may be due to the possibility of the PVE being countered by the semantic knowledge of the expert, or the gray values of the skull itself may vary significantly. Furthermore, the ground truth is scaled up by a factor of 4 compared to the original dataset. The scaling can result in the amplification of errors in the manual segmentation when rescaling the ground truth to match the resolution of the original slices. The interpolation method itself can also produce errors.

Additionally to the high dynamic range in the whole sequence, the slices do not show uniform illumination. Figure 3.2 shows the estimated bias fields for each slice in the

exemplary sequence *03*. For these results, MATLAB code provided on the MATLAB File Exchange by Li et al. [21] was modified and used to calculate slice-based bias fields.

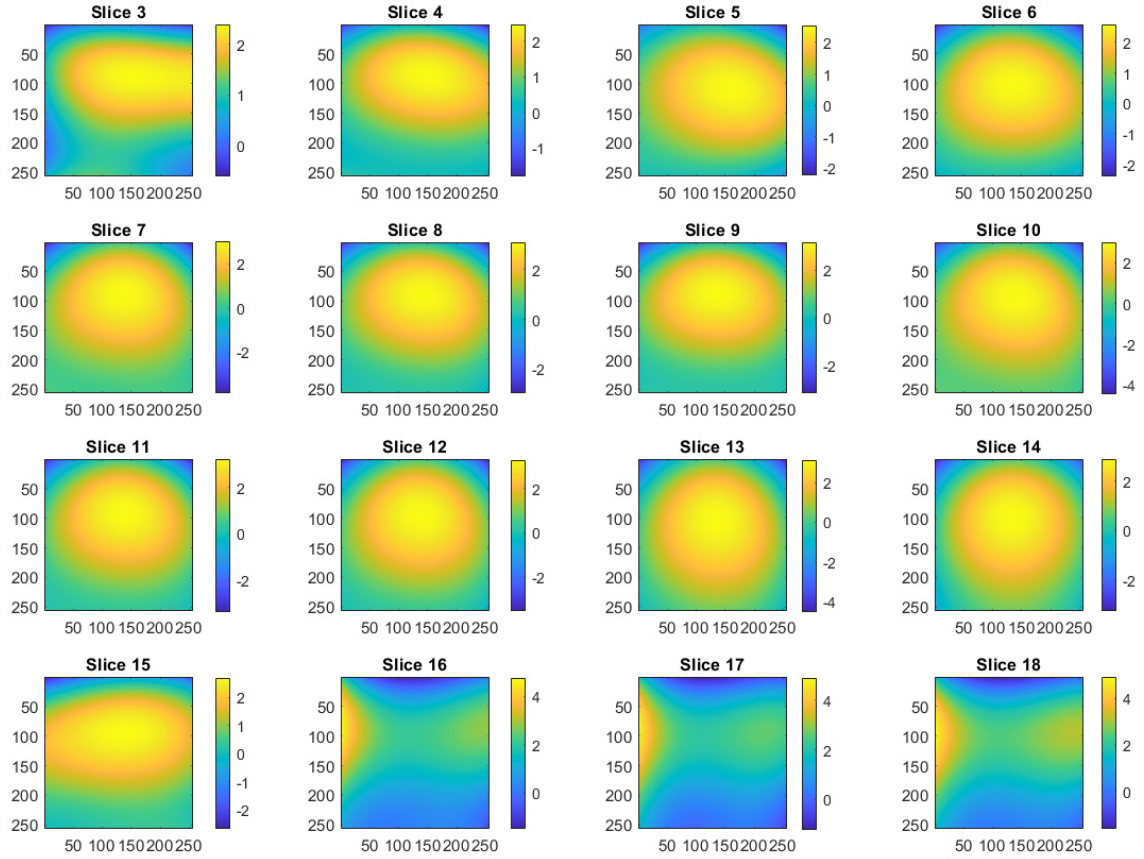


**Figure 3.2.:** Estimated bias field in slices of sequence *03* according to the bias field correction presented by Li et al. [21] (5 iterations).

In summary, the AuSoMS must perform automatic segmentation in cranial rodent MRI scans based on the following: The slices' illumination is not necessarily uniform, motion artifacts and PVEs may occur, and the skull can potentially be challenging to distinguish from other parts of the MR image due to the bad SNR. The segmentation should prioritize the skullcap. AuSoMS has to operate on a low amount of slices per sequence.

## 3.2. Read data

The data is available in the DICOM format. All files of a given directory are converted into a gray value matrix. The DICOM headers containing the values of slice thickness  $slt$  and the pixel dimension  $d_{pixel}$  are saved for further use. The gray values in the sequence are normalized to gray values in  $[0, 1]$  with a linear scaling operation. Because the normalization is applied to the entire sequence, the proportions of the gray values between slices are preserved. The normalization allows any input data types while avoiding the loss of information. After the normalization, an optional cutoff is applied to the sequence to ignore noisy posterior and anterior slices. FUS targets mostly the middle slices and

therefore in this thesis two anterior-most and two posterior-most slices are excluded from the segmentation. In the following text, the pixel values are based on a pixel spacing of  $d_{pixel,1} = d_{pixel,2} = 0.0781$  mm, where  $d_{pixel,1}$  is the scale of a pixel in the first dimension and  $d_{pixel,2}$  is the scale of a pixel in the second dimension.

## 3.3. Pre-processing

As shown in figure 1.1, the dynamic range of the whole sequence is high. This is due to the fact that the eyes in the posterior layers have a large signal amplitude compared to other tissues. As a result, the contrast between skin, brain, and bone is low in many slices. In addition, the bias fields entail that each slice is not evenly illuminated (see also figure 3.2), which reduces the contrast in lower areas of the slices. This section presents the methods used to improve the contrast before segmentation. The pre-processing is entirely slice-based, which means all methods are applied to each slice separately.

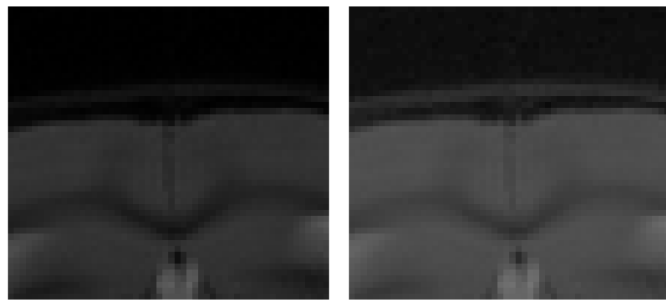
### 3.3.1. Histogram equalization

To adjust the contrast of the each slice, Contrast Limited Adaptive Histogram Equalization (CLAHE) for histogram equalization is used [42, 18]. CLAHE is a method intended to enhance low-contrast medical images. Instead of modifying the global histogram of the slice like in traditional Histogram Equalization (HE), the equalization is performed locally. This is known as Adaptive Histogram Equalization (AHE).

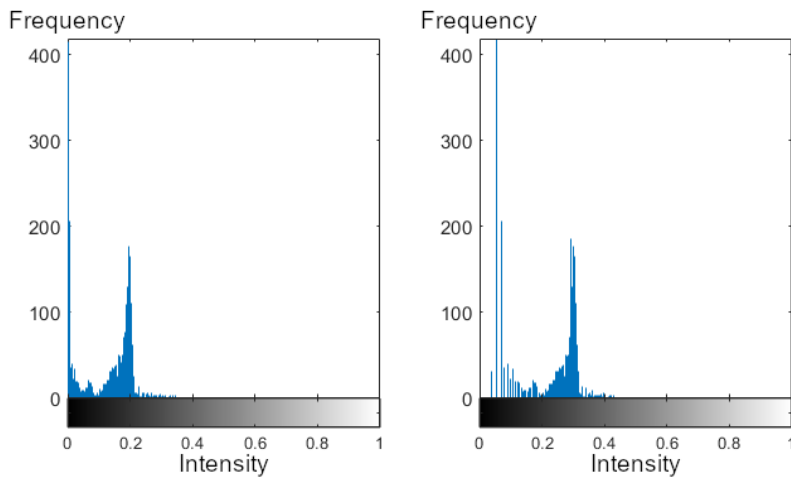
Additionally to the local histogram equalization, CLAHE enables contrast limiting to avoid the amplification of noise in homogeneous regions, which is a shortcoming of HE and AHE. After dividing the slice into non-overlapping blocks of size  $B \in \mathbb{N} \times \mathbb{N}$  and calculating the respective histograms, CLAHE clips the histograms at a predefined value  $L \in [0, 1]$  before computing the cumulative distribution function of the gray values of each block. The intensity values in each region are then enhanced with respect to a given distribution  $D(X)$  [22, 33].

The MATLAB implementation of CLAHE allows for uniform distribution, Rayleigh distribution, or exponential distribution. In this thesis, heuristic observations show that choosing  $D(X)$  as rayleigh distribution with distribution parameter  $\sigma = 0.4$  and a block size of  $B = 20 \times 20$  pixels provides reasonable results. Latter corresponds to a size of approximately  $1 \times 1$  mm. The pixel spacing is used to automatically calculate the mentioned block size such that AuSoMS performs equally on different resolutions. The clipping limit  $l$  is set to 0 to minimize amplification of noise and to avoid flattening of the histogram.

CLAHE improves the contrast between the skull and the surrounding tissue (figure 3.3). However, due to the strict contrast limiting, the resulting image still does not utilize the normalized gray value space  $[0, 1]$  entirely.



**(a)** Left to right: Cropped image section of original grayscale slice and the same section after application of CLAHE. Contrast between skin, background and skull-cap is improved.



**(b)** Left to right: Histogram of slice section depicted in 3.3a before and after application of CLAHE.

**Figure 3.3.:** Effect of the CLAHE application on the original slice 8 of sequence 03.

### 3.3.2. Contrast enhancement

Because the pre-processing is slice-based, the contrast enhancement is performed on each slice separately. After the application of CLAHE, contrast enhancement further improves the histogram of each slice globally. AuSoMS uses the MATLAB function *imadjust*<sup>1</sup> to map the curve of the histogram to the interval  $[0, 1]$  and further enhance the contrast between dark regions and bright regions of the slice. The default contrast enhancement saturates the bottom 1% and the top 1% of the entire gray value space without the loss of information.

### 3.3.3. Image denoising

The previous steps in summary perform a non-linear transformation of the gray values. The last step of pre-processing removes the distorted noise as much as possible. A wide variety of methods for denoising exist. Many of them achieve denoising based

<sup>1</sup><https://de.mathworks.com/help/images/ref/imadjust.html>, accessed 2021-04-28.

### 3. Methods

---

on averaging. But the method introduced by Buades et al. [4], also known as Non-local Means Filtering (NLMF), makes use of information about the neighborhood of each pixel. Therefore, a weight function  $w(i, j)$  with  $0 \leq w(i, j) \leq 1$  and  $\sum_j w(i, j) = 1$  for pixels  $i$  and  $j$  quantifies the similarity between the neighborhoods of pixels  $i$  and  $j$ . The higher the weight, the more similar are the neighborhoods in terms of gray values and geometry. The similarity is measured as a decreasing function of the weighted euclidean distance, which contributes to the robustness of NLMF and allows for inclusion of the neighborhoods' geometries. The new grayscale value  $s_{nlmf}(i)$  of pixel  $i$  is computed as a weighted average of all gray values in slice  $s$ ,

$$s_{nlmf}(i) = \sum_j w(i, j) \cdot s(j). \quad (3.1)$$

The MATLAB implementation of NLMF enables the limitation of the search area around a single pixel, which improves the computation time. In this thesis, a search window of  $11 \times 11$  pixels respective  $0.8591 \times 0.8591$  mm was used and the neighborhood size was set to  $3 \times 3$  pixels respective  $0.2343 \times 0.2343$  mm to take care of fine structures. A bigger neighborhood size leads to less detailed brain structure, which would be problematic for the upcoming steps.

Figure 3.4 shows the whole pre-processing procedure on 3 exemplary slices.

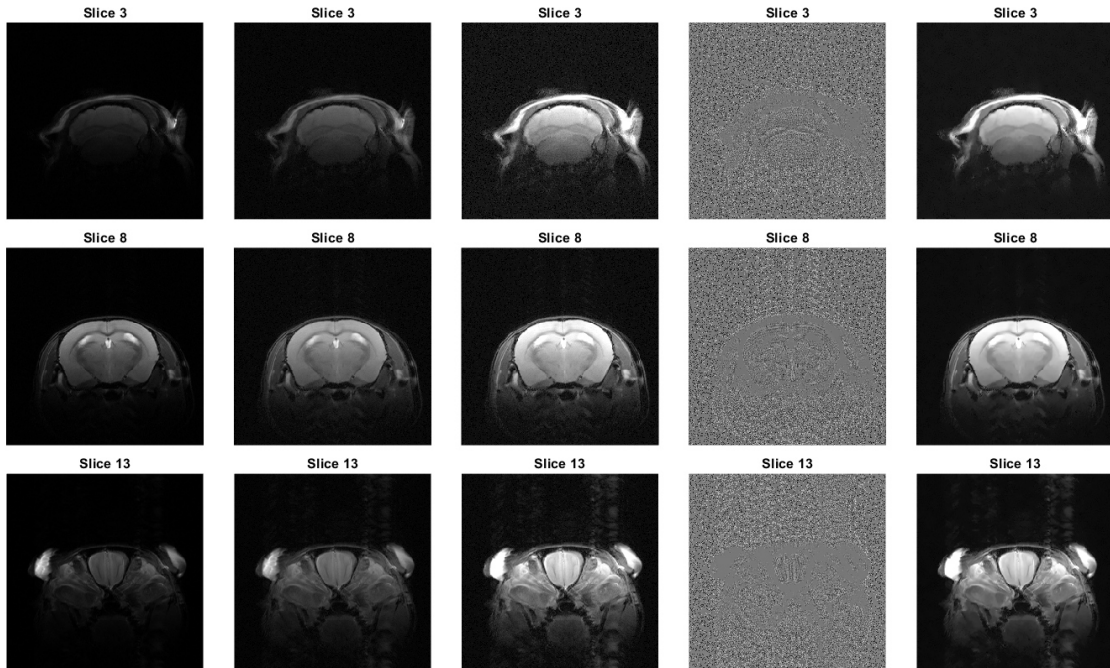


**Figure 3.4.:** Visualization of the pre-processing step using 3 exemplary slices. Each slice is processed independently. Columns depict - left to right - (i) Input slices (ii) after application of CLAHE (iii) after contrast enhancement (iv) difference between contrast enhanced slices and NLMF filtered slices (v) after application of NLMF.

## 3.4. Segmentation

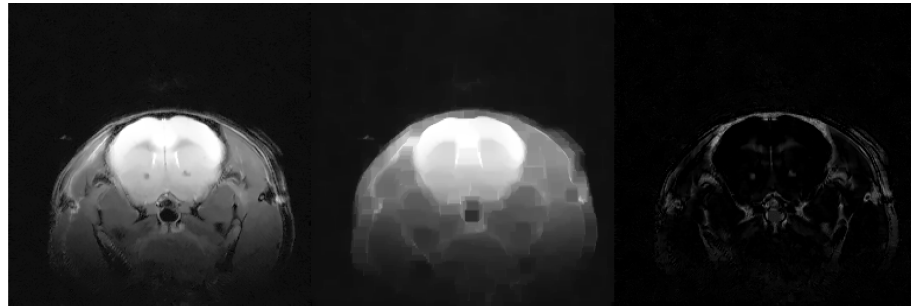
This chapter presents the segmentation of the pre-processed sequence. The segmentation makes use of slice-based and volume-based methods. Because bone tissue has a low signal in T2 weighted images, it is displayed darker in the slices with gray values similar to the background. The segmentation uses this property by segmenting the darker structures of the mouse head. Those dark structures in the head do not necessarily depict bone tissue exclusively. To improve the segmentation, the information about the anatomical position of the skull is used. Section 1.1 and prior observations in section 3.1 show that the region of interest is located around the brain. To make use of this information, AuSoMS uses a brain segmentation to locate the skull segments around the brain.

### 3.4.1. Foreground segmentation

To extract darker regions of the head, the head (foreground) is separated from the air surrounding the head (background). The foreground segmentation identifies the potential areas of the foreground which could represent the skull. The foreground segmentation uses morphological background removal to identify the foreground. Morphological operations are based on morphological mathematics. The important set operations besides intersection, union, difference, and complement are erosion and dilation. Erosion and dilation need a set, also known as structural element (SE), which defines the neighborhood of a pixel  $i$ . The gray values of the neighboring pixels are stored in a ranked order  $f$  based on intensity. The gray value of pixel  $i$  is adjusted depending on the type of morphologic operation [26].

Applying dilation assigns the maximum of  $f$  to pixel  $i$ , which emphasizes bright areas of the slice at the expense of darker areas. In contrast to this, erosion assigns the minimum value of  $f$  to pixel  $i$ , emphasizing the dark areas at the expense of lighter areas. The direction of this expansion depends on the shape of the SE. Applied to binary slices with values in  $\{0, 1\}$ , the dilation acts as logical AND (denoted with  $\wedge$ ) and the erosion acts as logical OR (denoted with  $\vee$ ). Erosion followed by dilation is referred to as *opening* and dilation followed by erosion is also known as *closing* [26].

Since the background of each pre-processed slice  $S$  is dark, the foreground segmentation applies a *closing* operation to emphasize the brighter structures of the slice. The shape of the SE is a disk since the shape of the head in each slice can be approximated by a circle. The morphological operation provides a closed slice  $SC$ , in which the foreground is bright. The dark structures of the head get concealed during the dilation phase of the *closing* operation. To retrieve the dark structures of the foreground,  $SC$  is subtracted from  $S$ . This step provides a grayscale slice  $FD = S - SC$  of the dark regions in the foreground (e.g. the skull, but also air-filled cavities). Figure 3.5a illustrates this process.



(a) Application of the morphological background removal. Left to right:  $S$ ,  $SC$ , and  $FD$



(b) Creation of the foreground mask. Left to right:  $FD_b$ ,  $FC_b$ ,  $D_b$ , and 4 largest segments of  $D_b$

**Figure 3.5.:** Foreground segmentation performed on slice 9 of sequence 03.

The goal is to produce a mask representing the dark structures in the foreground of the slice. To binarize an image, gray values below a certain threshold are classified as 0, and gray values equal or above the threshold are classified as 1. The Otsu's method [28] is an established method to calculate a specified number of thresholds in a grayscale histogram automatically. To binarize  $FD$ , the foreground segmentation uses the global calculation of one threshold based on [28]. To close holes in the resulting binary image, the foreground segmentation makes use of a *closing* operation. The structural element used for the *closing* operation is again a disk. The selection of the parameters for the morphological background removal and the subsequent *closing* of the mask is discussed in section 4.3. The result  $FD_b$  is just an approximate mask of the dark regions as the *closing* operation adds mass to each connected component in  $FD_b$  (figure 3.5b, outer left image). To correct this, the mask is combined with a mask  $FC_b$ .  $FC_b$  is created by using adaptive binarizing of the input slice  $S$ .

For the computation of the correction mask  $FC_b$ , the foreground segmentation applies adaptive binarizing to  $S$  and inverts the resulting foreground mask (figure 3.5b, center left image). Adaptive binarizing considers spatial variations in illumination and computes the threshold value for each pixel. The foreground segmentation uses the MATLAB implementation for adaptive binarizing using integral images. Integral images are used to reduce computation time [3]. The foreground polarity is defined as "dark" to account for the inhomogeneous illumination of the image during binarization. In this step, the dark regions are classified as 0 since the intensities are similar to the background. The resulting mask is inverted to classify the pixels of the dark regions as 1. The resulting slice  $FC_b$  is combined with  $FD_b$  to correct the segments ( $D_b = FD_b \cap FC_b$ , 3.5b, center right image).

The foreground segmentation detects all dark regions of the head. This includes bone tissue, cavities or dark structures of the brain. The skull is mostly shown as contiguous segment. However, since the skull segments do not necessarily consist of one large segment due to artifacts, the foreground segmentation extracts  $n = 4$  largest segments instead

of choosing the largest segment 3.5b, outer right image). The latter could work with the slice in figure 3.5b, for example, but not generally. Additionally, one foreground segment can contain bone tissue as well as other dark regions not representing the bone. Figure 3.6 features slices in which the dark regions of the brain are segmented and also shows segments containing multiple types of tissue.

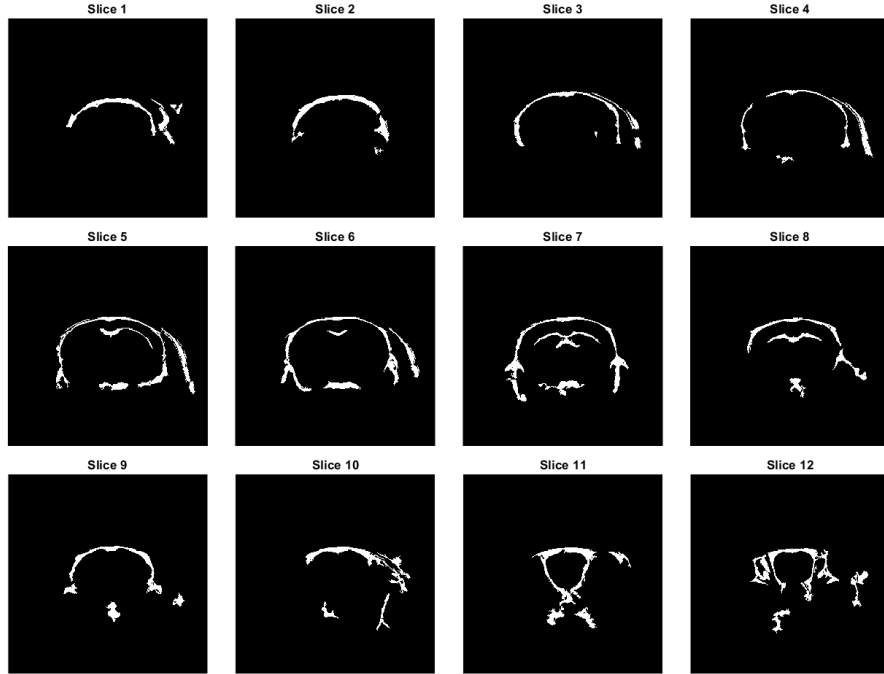


**Figure 3.6.:** Foreground segmentation of sequence 03.

As a consequence, there still are segments which do not represent the skull or contain tissue different from bone. Because the gray values in  $S$  of each segment in  $D_b$  are similar, the segmentation incorporates additional information about the anatomy of the mouse head and the properties of the segments to improve the segmentation.

### 3.4.2. Brain segmentation

Because the skull segments are located around the brain tissue, information about the brain region in the slice can be incorporated to remove tissue different from bone in from large segments. Additionally, AuSoMS excludes segments located too far from the brain. Furthermore, dark regions of the brain with similar gray values of the skull can be excluded. To retrieve this type of information, the brain has to be segmented automatically. The brain segmentation and the foreground segmentation process the pre-processed sequence independently.

#### 3.4.2.1. Bias field correction

Even though section 3.4.2.2 introduces a method for rodent brain segmentation which has built-in bias-field correction, observations show that an additional bias field correction

### 3. Methods

---

with Multiplicative Intrinsic Component Optimization (MICO) before the brain segmentation improves the segmentation result. The approach uses an implementation of the MICO algorithm to homogenize the illumination of the slice [21]. The MICO algorithm provides robust joint bias field correction and tissue segmentation. But since the tissue segmentation was only evaluated on human cranial MRI, only the bias field correction is utilized in the implementation of this thesis. The bias field correction iteratively optimizes the bias field of each slice separately. After 5 iterations the algorithm empirically computes satisfactory results.

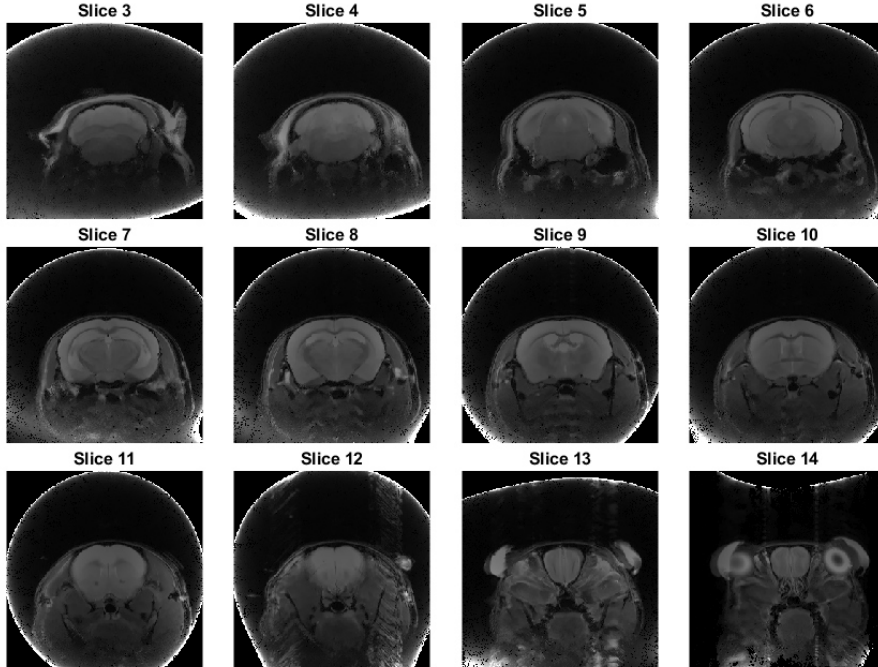


**Figure 3.7.:** Bias field corrected slices of sequence 03. The implementation utilizes code provided by Li et al. [21].

Figure 3.7 shows that the brain is illuminated homogeneously after the bias field correction. However, there occur artifacts at the outer regions of the slice due to MICO.

During the development of AuSoMS, attempts were made to use MICO as a pre-processing step. However, this worsened the results of the foreground segmentation described in section 3.4.1. The artifacts created by this method create additional bright regions in the background of the slices, which is a plausible reason for the poor outcome if MICO is applied before the foreground segmentation.

#### 3.4.2.2. 3D-PCNN segmentation

Chapter 2 shows that segmentation of brain tissue in rodent cranial MRI is already researched. Chou et al. [7] propose an algorithm capable of segmenting the brain tissue in rodent MRI scans automatically. The 3D-PCNN algorithm extends a robust Pulse-coupled Neural Network (PCNN) algorithm proposed by Murugavel and Sullivan [24]. 3D-PCNN is robust to noise and irregular boundaries. Additionally, it does not require training. 3D-PCNN also considers neighboring information across slices and needs a volume as input.

The algorithm can process non-isometric data, because the voxel dimension is scalable to the actual voxel dimension. AuSoMS automatically calculates the voxel dimension  $d_{voxel}$  of each input sequence assuming the pixel spacing  $d_{pixel}$  is isometric and using the slice thickness  $slt$ ,

$$d_{voxel} = d_{pixel,1} \times d_{pixel,2} \times slt. \quad (3.2)$$

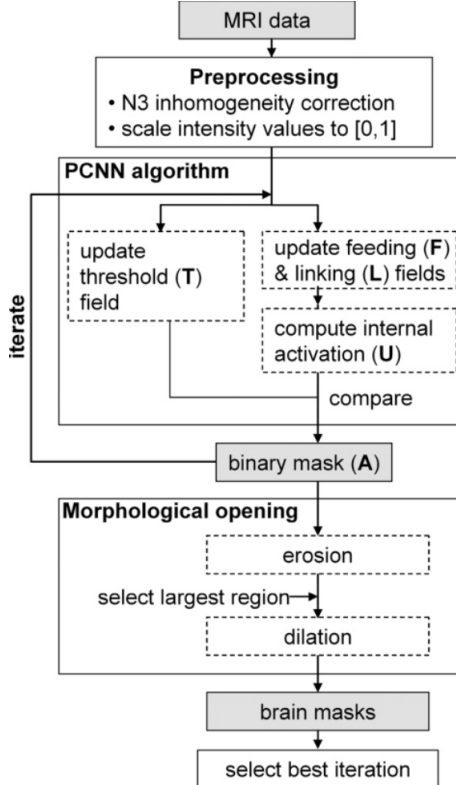


**Figure 3.8.:** Processing flow of 3D-PCNN as shown in [7].

3D-PCNN assumes that the brain is the largest continuous structure in the sequence. Each iteration produces a brain mask. The volume of the brain mask is calculated with the respective voxel volume. Each iteration performs a morphological operation and connects large continuous regions. Morphological dilation is applied by the 3D-PCNN algorithm to restore the size of the brain mask. AuSoMS chooses a SE size of 5 px respective 0.3905 mm. Section 4.2 shows in detail how this choice is made. The brain mask is passed to the next iteration, in which more regions in the volume are counted as brain regions. Figure 3.9 shows the brain mask volume plotted against the iteration number. If the volume of the brain mask volume exceeds 800 mm<sup>3</sup>, the 3D-PCNN algorithm stops the loop. This is reasonable because the brain volume is assumed to be between 100 mm<sup>3</sup> and 550 mm<sup>3</sup>. Typically there is a steep increase of the brain mask volume towards the end, which is why the termination condition is 800 mm<sup>3</sup> instead of 600 mm<sup>3</sup>, for example (figure 3.9, E). The algorithm estimates the optimal iteration automatically. The optimal iteration can be found in the plateau region of the plot (figure 3.9, C). Within a specified range of 100 mm<sup>3</sup> – 550 mm<sup>3</sup>, the iteration number with the largest increase in brain mask volume and largest decrease respectively are identified (figure 3.9, A-B and D-E). The iteration residing in the middle of these two iterations is chosen to be the optimal iteration.

### 3. Methods

---

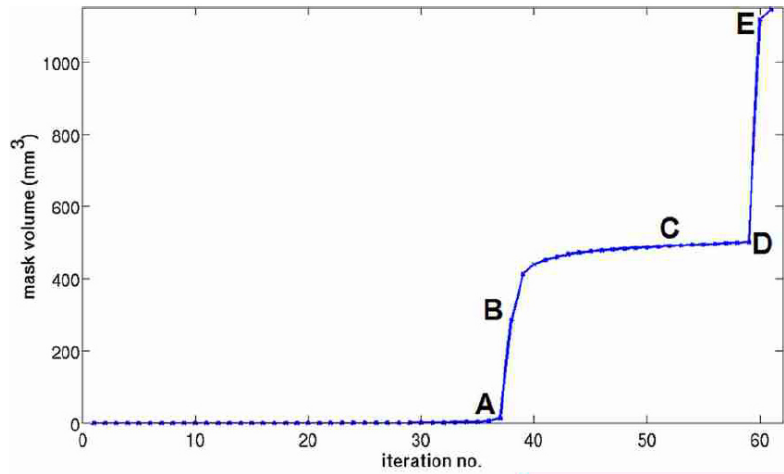


**Figure 3.9.:** Brain mask volume plotted against iteration number as shown in [7].

#### 3.4.2.3. Post-processing of the brain segmentation

The 3D-PCNN method provides reasonable results as depicted in 3.10. However, the brain volume also contains parts of the slices that represent the eyes and some areas around the brain. This can be due to the cutoff applied to the sequence and accompanying loss of brain information in the whole sequence. A missing plateau in the brain volume, the ample spacing between slices or the highly distorted voxel dimensions are additional sources of error.

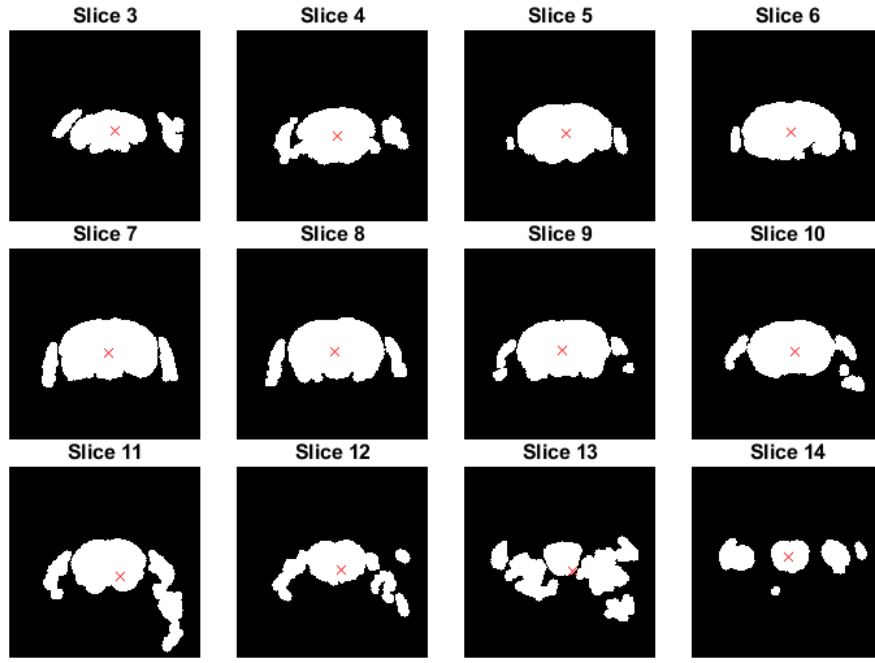


**Figure 3.10.:** Exemplary brain segmentation of sequence 03. The centroids are marked red. Only the underlying segment is selected.

To address this issue, AuSoMS utilizes the symmetry of the head structures. The post-processing step of the brain segmentation calculates the centroid of the pixels labeled as

1 of each slice in the brain mask. Generally, the centroids are located in the correct brain segment of the slice. AuSoMS chooses only the corresponding brain segment to remove the incorrectly classified pixels and thus improves the brain segmentation. The brain segmentation generates a brain mask sequence the same size as the MRI sequence with applied cutoff.

### 3.4.3. Skull segmentation

For the skull segmentation, AuSoMS merges the foreground segmentation of section 3.4.1 and the brain segmentation of section 3.4.2. In addition, the skull segmentation assesses the remaining segments according to their spatial properties.

The brain segmentation  $B$  enables removal of structures actually belonging to the brain in each slice of the foreground segmentation  $F$ . Because both segmentation volumes are sequences of binary masks, the skull segmentation performs the logical operation

$$\tilde{F} = F \wedge \neg B. \quad (3.3)$$

The operation removes the dark structures of the brain in the foreground segmentation. Furthermore,  $B$  is used to identify pixels not representing the skull. The skull thickness varies based on gender, weight, and age of the mouse. The maximal skull thickness is defined as  $st_{max} := 0.7$  mm [15]. The implementation uses information about the pixel spacing to create a region of interest (ROI)  $R$ . For the creation of  $R$  each slice  $B_i$  of the brain mask is dilated with a SE size of

$$SE_{roi} = \lceil \frac{st_{max}}{d_{pixel,1}} \rceil, \quad (3.4)$$

and  $B$  is subtracted from the sequence of dilated masks  $B_{dil}$  (eq. 3.5),

$$R = B_{dil} \wedge \neg B. \quad (3.5)$$

Every pixel of the foreground segmentation labeled as 1 in the ROI is interpreted as part of a skull segment. Therefore, the mask  $R$  is intersected with the foreground mask  $\tilde{F}$ .

$$F_{roi} = \tilde{F} \wedge R. \quad (3.6)$$

Figure 3.11 represents an exemplary combination of foreground segmentation and brain segmentation.

### 3. Methods

---

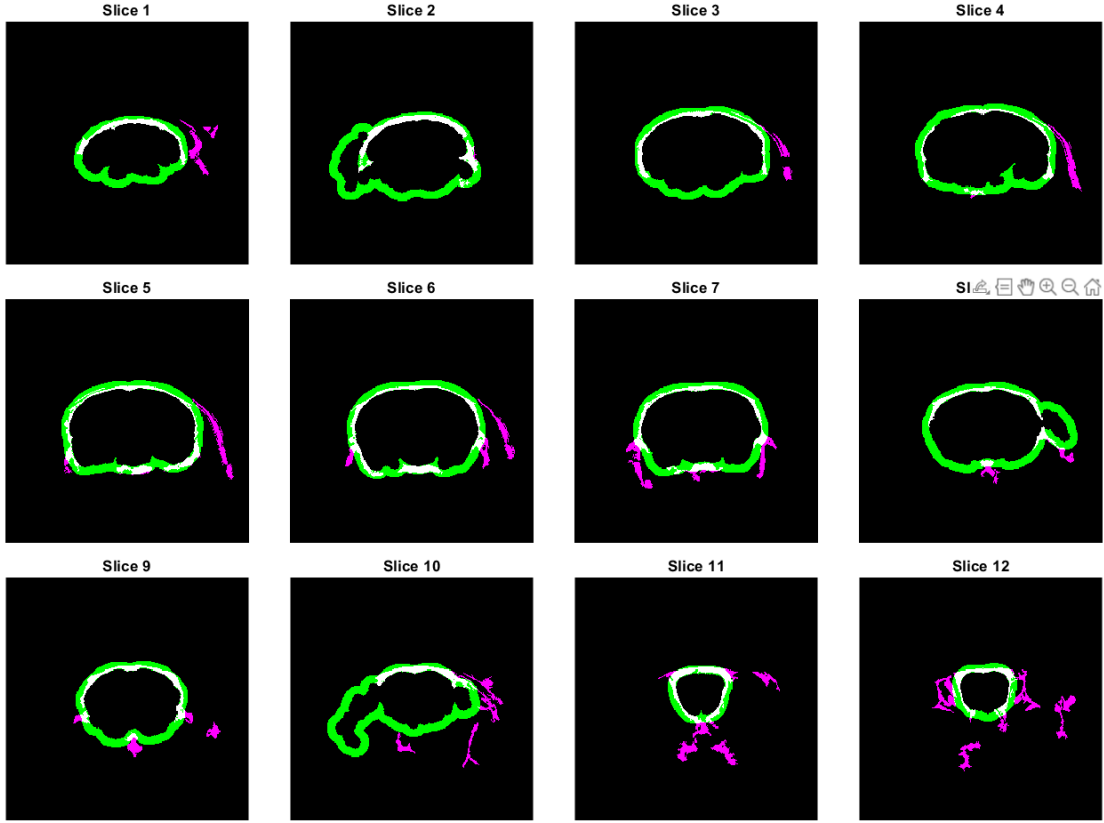


**Figure 3.11.:** Combination of brain segmentation and foreground segmentation. The respective segments are color-coded. Magenta:  $\tilde{F}$ . Green:  $R$ . White:  $F_{roi}$ .

Because the combination of  $R$  and  $\tilde{F}$  does not select entire segments but pixels, small fragments can be formed. As the ROI only accounts for the maximum skull thickness and the brain segmentation can overestimate the brain (see also figure 3.11), there still are pixels not representing bone tissue in  $F_{roi}$ . To remove them, every connected component in a slice of  $F_{roi}$  is interpreted as an object and assessed on the basis of the spatial properties.

Skull objects typically are thin, curved, and oblong segments. As a consequence, the convex hulls of the skull objects are more ellipsoidal. Also, they are usually larger than the fragments. This property can be used to distinguish skull objects from fragments. To classify objects as either skull objects or fragments, AuSoMS uses a metric describing the size of an object. The Feret diameter is an appropriate unit of measurement of the size of an object.

The Feret diameter is determined by measuring the distance between two parallel vertices which enclose the object at a specified angle. For each object, the skull segmentation measures the maximal distance between these vertices, which is also known as the maximum Feret diameter. The maximum Feret diameter brings out the different sizes of the segments better than the minimal Feret diameter and emphasizes the elongated shape of the skull segments. Figure 3.12 illustrates the measurement of the Feret diameter.

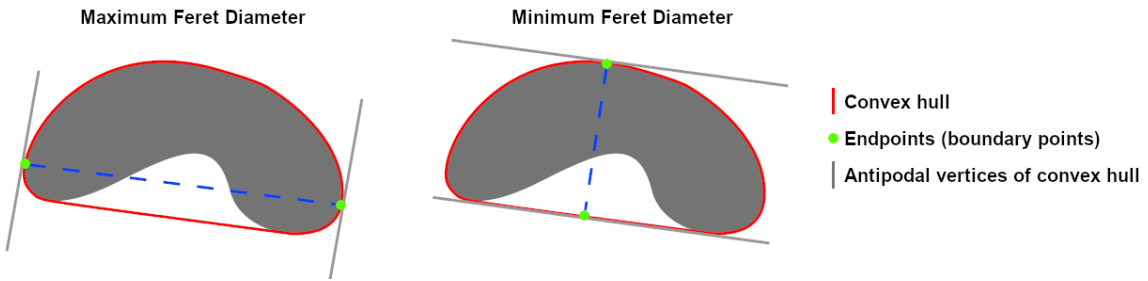


**Figure 3.12.:** Illustration: Measurement of the maximum Feret diameter and the minimum Feret diameter. Adapted from <https://de.mathworks.com/help/images/ref/bwferet.html>, accessed 2021-05-01.

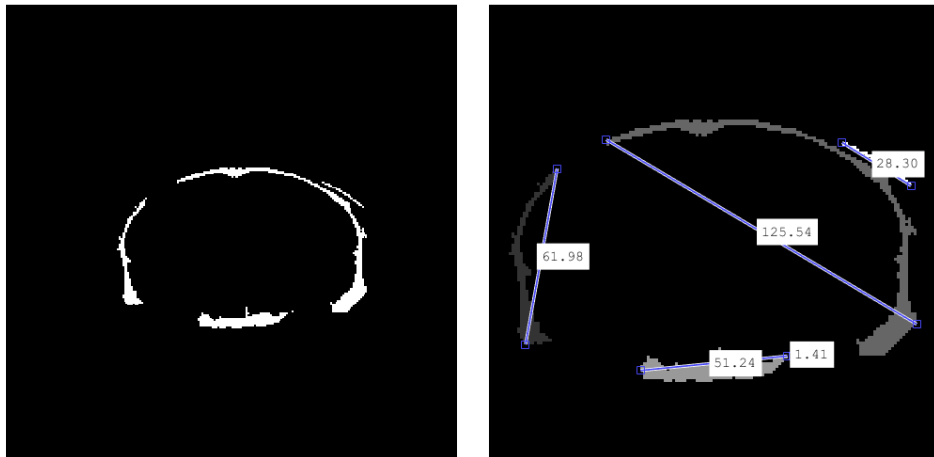


**Figure 3.13.:** Measurements of the maximum feret diameter in pixels of all objects in an exemplary slice of  $F_{roi}$ .

Every object with a maximum feret diameter of 0.4 mm and above is classified as a skull segment. Most likely, the heuristically chosen threshold of 0.4 mm is not optimal. However, the location of the artifacts in the MRI leading to the division of the skull segment into multiple segments is not statistically recorded in this thesis. Because the optimal choice of the threshold is unknown, the goodness of this selection can not be specified.

Nevertheless, small fragments can be removed with this threshold. The resulting sequence is defined as  $\tilde{F}_{roi}$ . However, there still are segments with a large enough maximum Feret diameter which do not represent the skull. These segments are interpreted as outliers. Despite the large slice thickness, the actual skull segments of each slice overlap with the skull segments of neighboring slices. In contrast, this does not apply to the outliers. AuSoMS makes use of the spatial information to identify outliers.

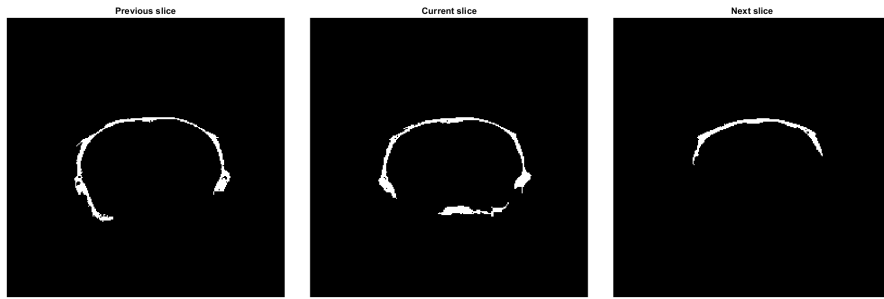
The idea is to ignore all segments which are not overlapping with any segments in the direct neighboring slices. For each slice, the geodesic distance of the segments to the segments of the neighboring slices is calculated with the MATLAB function *bwdistgeodesic*.<sup>2</sup> This calculation is performed for each neighboring slice separately (3.14b, left and middle image). If a segment in the current slice does not overlap with a segment in the

<sup>2</sup><https://de.mathworks.com/help/images/ref/bwdistgeodesic.html>, accessed 2021-04-28.

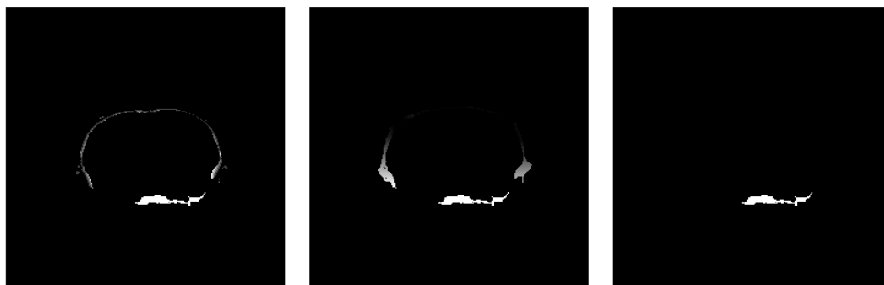
### 3. Methods

neighboring slice, the geodesic distance of each pixel in the corresponding segment is set to *Inf*. This value is used to identify pixels in the current slice which reside in a segment not overlapping with any segments in the neighboring slices (3.14b, right image). These pixels are then excluded from the segmentation. Consequently this procedure removes outliers. Pixels of the background get the result *NaN*, so they can be distinguished from pixels of the segments.

The corrected slices are written back into the sequence  $\tilde{F}_{roi}$ . The resulting sequence is the output of the skull segmentation. Algorithm 2 shows the procedure of outlier correction.



**(a)** Left to right: Previous slice, current slice, and next slice in sequence  $\tilde{F}_{roi}$



**(b)** Segments of current slice in figure 3.14a. Left to right: Geodesic distance to previous slice, geodesic distance to next slice, and segment not overlapping with at least one segment in the neighboring slices.

**Figure 3.14.:** Outlier correction on an exemplary binary mask.

## 3.5. Post-processing

The skull segments are mostly contiguous around the brain. But observations show a frequent division of the skull segment in two parts. This is possibly due to the artifacts or the occurrence of bad contrast in thin areas of the skull. Post-processing therefore connects gaps between 2 segments up to and including a certain threshold width  $t$ .

For this purpose, two images are generated only containing one segment of the  $n$ -th slice  $\tilde{F}_{roi,n}$  respectively. Therefore, the MATLAB function *bwconncomp* is used.<sup>3</sup> For each pixel classified as 0 in the images, the distance to the next pixel classified as 1 is calculated (MATLAB function *bwdist*<sup>4</sup>). The distances of the pixel in both images

<sup>3</sup><https://de.mathworks.com/help/images/ref/bwconncomp.html>, accessed 2021-04-27.

<sup>4</sup><https://de.mathworks.com/help/images/ref/bwdist.html>, accessed 2021-04-28.

are added. The resulting matrix contains the length of a path linking both segments. The calculation of the matrix's global minimum  $minDist$  allows for localization of the shortest path between the segments. In order to close the gap, a goodness  $g$  (in pixels) has to be defined which represents the allowed deviation from the shortest path. All pixels with a distance of  $minDist + g$  are then classified as 1 in the original slice  $\tilde{F}_{roi,n}$ . Since this method does not take into account curvature of the scullcap, the gap is only closed if

$$\lceil \frac{minDist}{d_{pixel,1}} \rceil \leq t, \quad (3.7)$$

to avoid unrealistic approximations of the bone tissue. AuSoMS empirically defines  $t = 1.5$  and  $g = 0.5$ . Because no division of the skullcap into more than two segments could be observed, the implementation is limited to only close the gap in case the skull segmentation consists of two segments. Algorithm 3 shows the procedure of the gap closing. The post-processing concludes the methods used for the automatic segmentation.

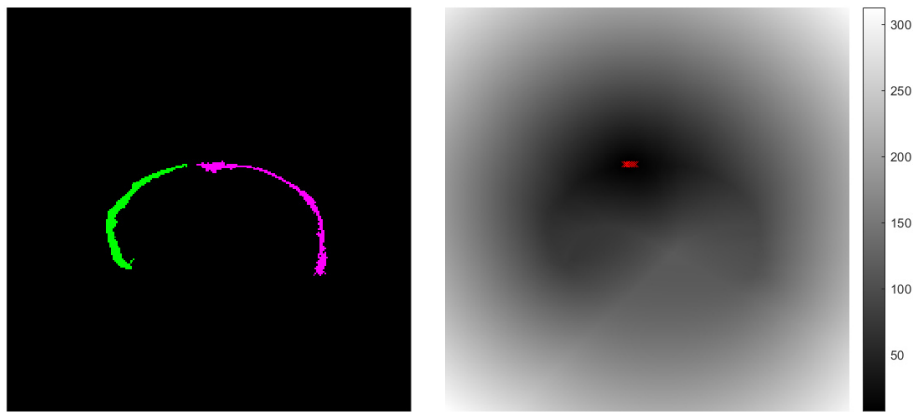


**Figure 3.15.:** Exemplary slice in which the skull consists of two segments. Left: Two segments of a slice showing a small gap in the skullcap. Right: The according matrix containing the path lengths. The brighter the gray value, the higher the length of the path linking both segments. Red markers show pixels residing on the shortest path.

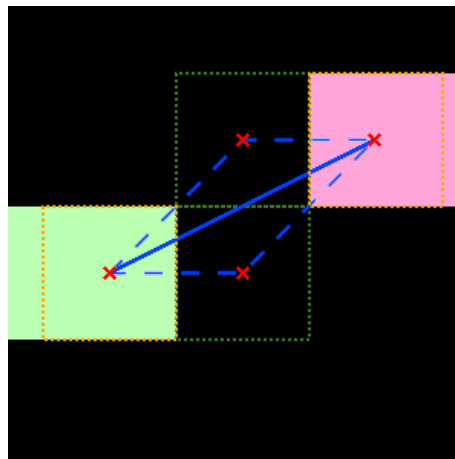


**Figure 3.16.:** Close-up view of an exemplary gap between two segments. Red crosses mark the center of each pixel which will be added to the segmentation. Because the direct path (blue) only contains pixels of the segments (orange), a goodness has to be defined to close the gap (dotted blue).

# 4. Results

This chapter shows the behavior of the implementation and analyzes it. Section 4.1 introduces two different metrics that, according to their respective significance, are used in optimization and evaluation to assess the quality of the results. Labeled ground truth data is provided by one rater. The ground truth provides brain segmentation and skull segmentation. Evaluation and optimization use the ground truth data as a reference. Section 4.5 briefly discusses the computational complexity of the segmentation.

## 4.1. Metrics

To optimize the parameters and evaluate the results, the quality of the segmentation output has to be quantified. As each segmentation performed by AuSoMS can be interpreted as binary classification, this section details two metrics used for quality assessment of binary classifiers.

$U = \{0, 1\}$  is the set of logical elements. Let  $S$  be the segmented data set and  $G$  the logical ground truth data set consisting of elements in  $U$ . Pixels in segmented data classified as  $1 \equiv \text{positive}$  are grouped in set  $S_p$ , pixels in segmented data classified as  $0 \equiv \text{negative}$  are grouped in set  $S_n$ , pixels in ground truth classified as *positive* are grouped in set  $G_p$  and pixels in ground truth data classified as *negative* are grouped in set  $G_n$ . The confusion matrix is defined as  $M = \begin{pmatrix} TP & FN \\ FP & TN \end{pmatrix}$  with classes

$$TP = |S_p \cap G_p| \quad \text{true positive,} \quad (4.1)$$

$$FN = |S_n \cap G_p| \quad \text{false negative,} \quad (4.2)$$

$$FP = |S_p \cap G_n| \quad \text{false positive,} \quad (4.3)$$

$$TN = |S_n \cap G_n| \quad \text{true negative.} \quad (4.4)$$

These four classes form all possible outcomes for a binary classification. The confusion matrix  $M$  is used to calculate a scalar representing the quality of the segmentation. There exist many metrics, but for image processing and medical image segmentation the following appear frequently in the literature.

### 4.1.1. Dice score

The Dice score is a particular form of the F-Score. The F-Score is the harmonic weighted mean of recall  $R$  and precision  $P$ . Recall denotes the percentage of  $TP$  out of the amount of pixels  $|G_p|$  classified as positive in the ground truth. Therefore, recall can reward inaccuracy (recall is perfect if simply every pixel is classified as positive). Precision denotes the percentage of  $TP$  out of the amount of pixels  $|S_p|$  classified as

## 4. Results

---

positive in the segmentation. Precision can reward under-estimation. Used individually, recall and precision do not represent a balanced metric.

The F-Score combines recall and precision to form a balanced metric [9, eq. 4],

$$P = \frac{TP}{TP + FP}, \quad R = \frac{TP}{TP + FN}, \quad F_\beta = (1 + \beta^2) \cdot \frac{P \cdot R}{\beta^2 \cdot P + R} \in [0, 1]. \quad (4.5)$$

The higher the weight  $\beta$ , the more recall is favored above precision. The  $F_1$  score is equivalent to the Dice score [6]. The Dice score is a widely used metric for the evaluation of medical image segmentation methods [6, 27, 19]. The adapted formula introduced by Zijdenbos et al. [41, sec. V] for the Dice score is

$$\text{Dice} = \frac{2TP}{2TP + FP + FN} \in [0, 1]. \quad (4.6)$$

### 4.1.2. Matthews Correlation Coefficient

The Dice score provides reliable results if the segmentation correctly respective incorrectly identifies both positive and negative classes. But they can be misleading if the segmentation performs well just with either negatives or positives. The Matthews Correlation Coefficient (MCC) is a robust statistical measure which can address this issue [6]. The non-normalized MCC is defined as

$$MCC = \frac{TP \cdot TN - FP \cdot FN}{\sqrt{(TP + FP) \cdot (TP + FN) \cdot (TN + FP) \cdot (TN + FN)}} \in [-1, +1]. \quad (4.7)$$

Equation 4.7 calculates the Pearson product-moment correlation between the actual and predicted values. The result is  $+1$  for a perfect classification,  $-1$  for a perfect misclassification and  $0$  for a coin tossing classifier. The MCC is only high if the segmentation was able to correctly classify the majority of positives and the majority of negatives.

## 4.2. Optimization of the brain segmentation

Before the evaluation of the final results, the preceding steps are examined and optimized. The optimization of the brain segmentation is concluded independently from the rest of the steps. Furthermore, the parameters for the two morphological operation of the foreground segmentation are optimized.

Section 3.4.2.2 introduces a parameter for the size of the structuring element used by the morphological operation included in the 3D-PCNN method. Chou et al. [7] suggest a size of 4 pixels. However, the specifications of the available data for this thesis differ from theirs.

This section aims to identify the optimal size  $SE_{brain}$  for the structuring element in the brain segmentation. For each selection of  $SE_{brain}$ , the Dice score and the MCC score are calculated for the brain segmentation using the ground truth data. Additionally, the 3D-PCNN method entails a random component for a fixed parameter. To look at the effects of this component,  $N = 1000$  repetitions were performed per selected parameter. Both scores were calculated for each repetition. For each sequence, the two anterior-most

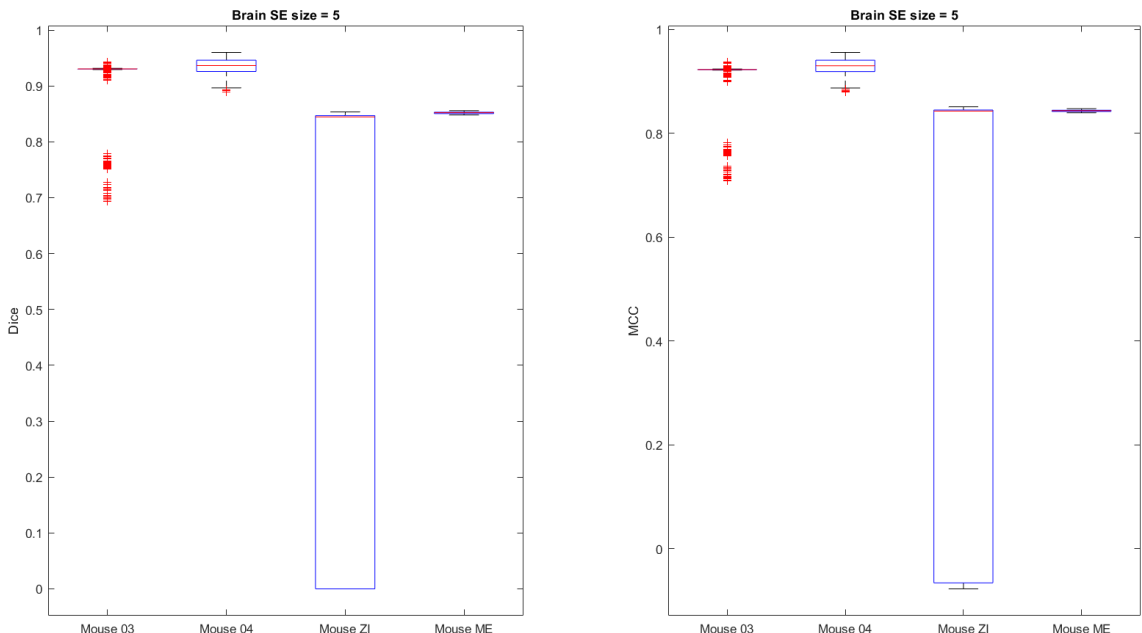
and the two posterior-most slices were excluded. The slices were scaled to  $256 \times 256$  pixels and the segmentations were performed with a selection  $SE_{brain} \in \{4, 5, 6, 7, 10\}$ .

Figure 4.2 shows the median scores for the brain segmentation with a fixed parameter on all four sequences. For all metrics the best median score is achieved using the SE size  $SE_{brain} = 5$ , while larger SE sizes tend to achieve lower scores for each metric. Therefore, this selection is considered to be optimal.

Figure 4.1 shows the results for the optimal selection of  $SE_{brain}$  in detail. The scattering due to the random component of the brain segmentation varies for each sequence. Figures B.5, B.6, B.7, and B.8 show the detailed results for every other selection of  $SE_{brain}$  in  $\{4, 6, 7, 10\}$ .

The bottom border of the blue boxes mark the 25%-percentile  $q_1$ , the top border of the blue boxes mark the 75%-percentile  $q_3$ . The horizontal red lines mark the median values. An observation  $O_i$  is considered as outlier and marked as red plus sign if

$$O_i < q_1 - 1.5 \cdot (q_3 - q_1) \vee O_i > q_3 + 1.5 \cdot (q_3 - q_1). \quad (4.8)$$



**Figure 4.1.:** Evaluation of the brain segmentation for all sequences with  $SE_{B_g} = 5$ .

## 4. Results

---

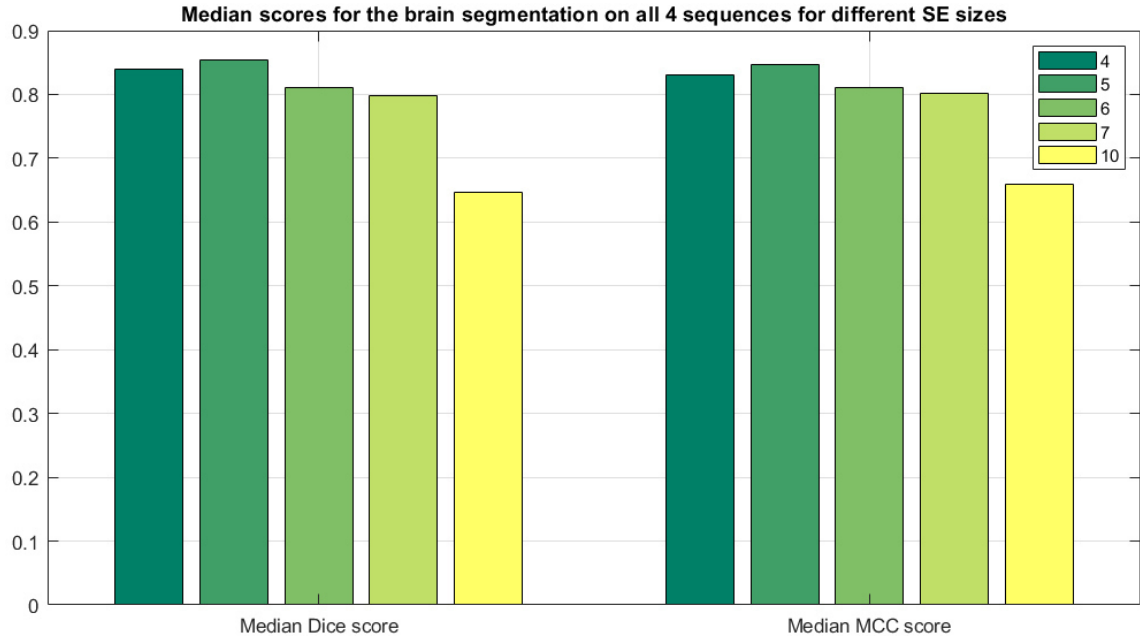


**Figure 4.2.:** Median scores for the brain segmentation on all 4 sequences for different SE sizes. The median of each score is highest for selection  $SE_{brain} = 5$ .

Figure 4.1 shows high medians above 0.9 for the most representative sequences 03 and 04. The variance  $v$  is less than 0.01 for all scores except from the scores for sequence ZI. The variance of the Dice score for sequence ZI is  $v_{diceZI} = 0.1556$  and the respective variance of the MCC score is  $v_{mccZI} = 0.1810$ . Although the variance of sequence ZI is high, the median value still is close to the 75%-percentile.

The variances are calculated using the MATLAB function `var` ignoring *NaN* values representing invalid results (eq. 4.9).<sup>1</sup>

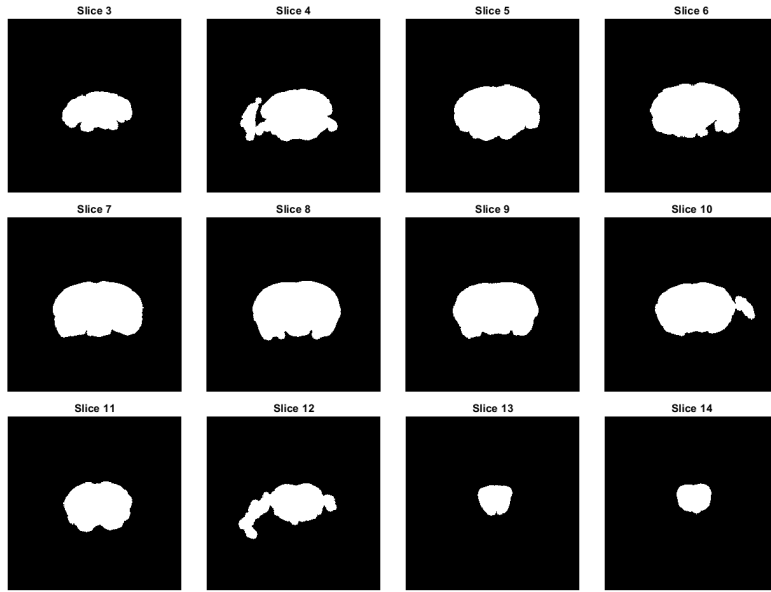
$$v = \frac{1}{\tilde{N} - 1} \cdot \sum_{i=1}^{\tilde{N}} |O_i - \hat{O}|^2, \quad (4.9)$$

$$\hat{O} = \frac{1}{\tilde{N}} \cdot \sum_{i=1}^{\tilde{N}} O_i.$$

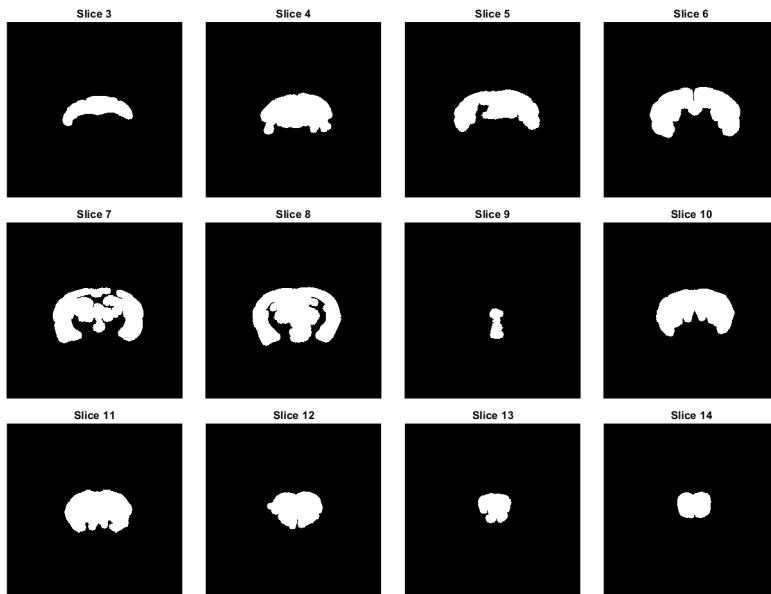
$O$  is a vector of observations for one type of score on a single sequence and  $\tilde{N}$  the amount of observations which do not equal *NaN*. *NaN* values in an observation represent a failure of the brain segmentation caused by an internal error of the 3D-PCNN algorithm. During all 20000 repetitions ( $4$  [sequences]  $\cdot$   $5$  [SE sizes]  $\cdot$   $1000$  [repetitions]), the internal error occurred two times. As a consequence, the *NaN* values do not have a significant influence on the overall result.

---

<sup>1</sup><https://de.mathworks.com/help/matlab/ref/var.html>, accessed 2021-04-27.



(a) Exemplary brain segmentation with Dice score and MCC score of  $> 0.9$ , close to the median score values.



(b) Exemplary brain segmentation with Dice score and MCC score of  $< 0.8$ .

**Figure 4.3.:** Comparison between a rather good brain segmentation and a worse brain segmentation of the same sequence 03.

To address the issue of the large variance, the additional goal of the brain segmentation optimization is the compensation of the variance. Therefore, the optimization utilizes the high median scores of the results. Because of the high median scores, the segmentation is expected to perform well in most cases. A bad brain segmentation tends to underestimate the brain or shows empty brain mask slices. Figure 4.3 shows two different results of the brain segmentation. An example of a bad brain segmentation is depicted in figure 4.3b.

## 4. Results

---

The first idea is to calculate a number of segmentations per iteration and automatically select the best brain mask. For this purpose, AuSoMS introduces a method selecting the best brain mask slices which does not need ground truth data (algorithm 1). The algorithm uses the number of ones in each slice of each brain segmentation to infer the average segmentation which has an expected high median score as shown in 4.1.

The algorithm works slice based. The pre-processed input sequence  $s$  is segmented 10 times with the fixed parameter  $SE_{brain}$ . For each slice position of the brain segmentation, the individual brain mask slices of all brain segmentations are considered. For each slice position the average number of ones of the brain mask slice in this position is calculated. The brain mask slice whose number of ones most closely corresponds to the average number of ones is selected.

---

### Algorithm 1 Variance compensation

---

**Require:**  $s, SE_{brain}$

```

1: segmentations  $\leftarrow \emptyset$ 
2: result  $\leftarrow \emptyset$ 
3: for  $n = 1, \dots, 10$  do
4:   segmentations( $i$ )  $\leftarrow$  3DPCNN( $s, SE_{brain}$ )
5: end for
6: for  $i = 1, \dots, numSlices$  do
7:    $avg \leftarrow 0$ 
8:   for  $j = 1, \dots, 10$  do
9:     mask  $\leftarrow$  segmentations( $j$ ), mask at position  $i$ 
10:     $avg \leftarrow avg + COUNTONES(mask)$ 
11:   end for
12:    $avg \leftarrow avg / numSlices$ 
13:   result( $i$ )  $\leftarrow$  GETBESTSLICE(segmentations,  $avg, i$ )
14: end for

```

---

Figure 4.4 shows the results when using the newly introduced method with the selection of  $SE_{brain}$  resulting in the best average Dice score and MCC score. The method does not improve the results significantly.

The new variance of the Dice score for sequence  $ZI$  is  $v'_{diceZI} = 0.1527$  and the respective new variance of the MCC score is  $v'_{mccZI} = 0.1776$ . The new mean value of the Dice score is 0.8210 instead of 0.8196 and the new mean value of the MCC score is 0.8101 instead of 0.8085.

In future, this method could be evaluated with more than ten repetitions or replaced with a better method using another metric. Because of the lacking improvement and due to computation time considerations, the evaluation of the final results in section 4.4 uses a default value of 1 for the number of brain segmentations per skull segmentation to achieve the same behavior like without the usage of the variance compensation.

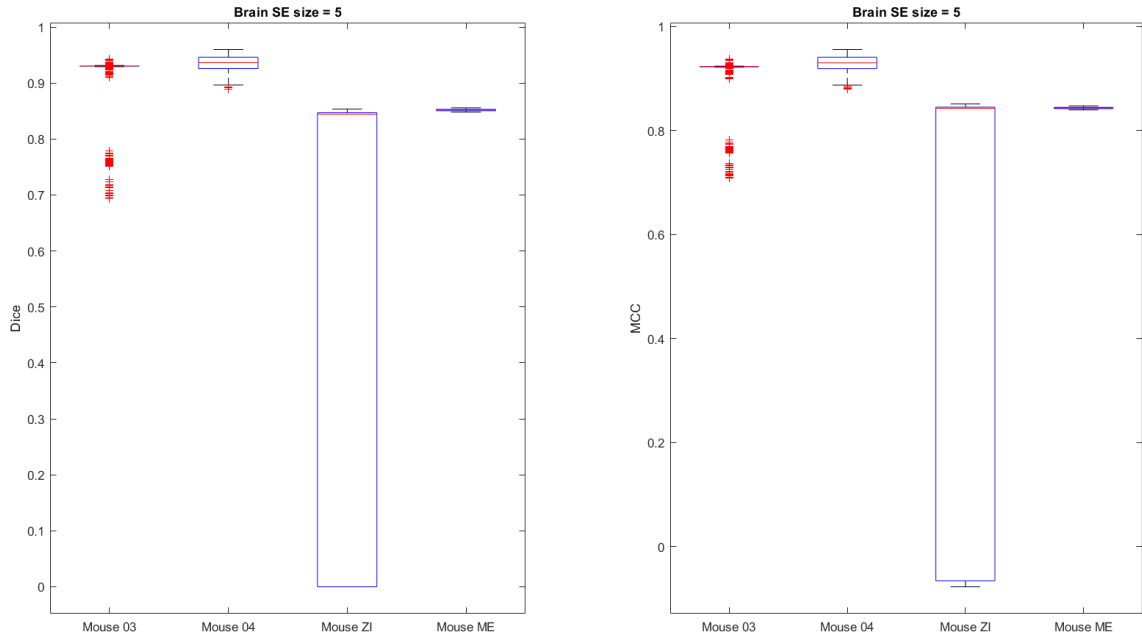


**Figure 4.4.:** Evaluation of the brain segmentation for all sequences using the introduced algorithm 1 for variance compensation.

## 4.3. Optimization of the foreground segmentation

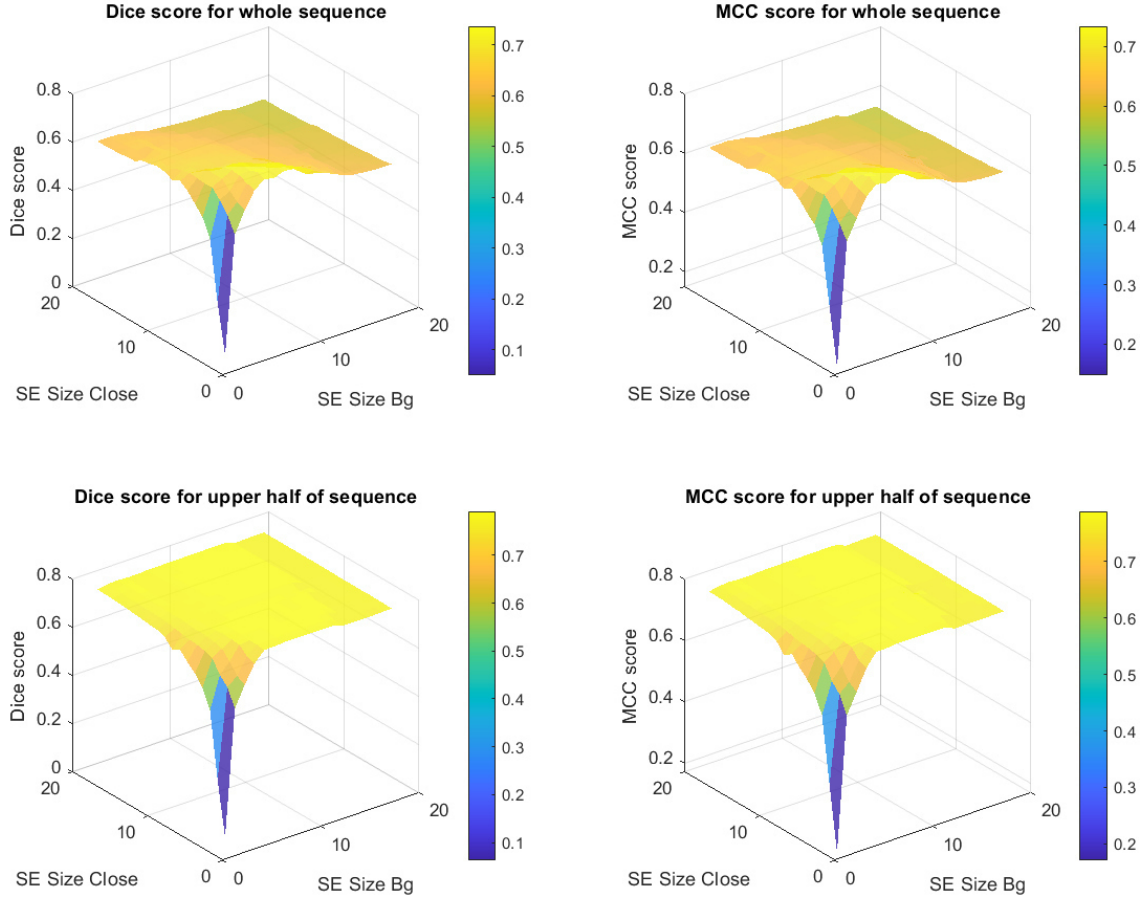
For the more detailed study of the behavior of the foreground segmentation, it is assumed that the brain segmentation performs perfectly. Therefore, the brain ground truth data is used to mimic the brain segmentation. Two parameters of the foreground segmentation are selected and the behavior of the entire segmentation is observed.

This section aims to optimize the SE sizes for the foreground segmentation explained in section 3.4.1. For each segmentation, the scores are calculated on the whole segmentation. The skullcap is the most important skull structure for the purpose of the HEiKA project. Therefore, the segmentation of the skullcap is of special interest in this thesis. Because the skullcap is depicted in the upper half of each sequence, the score is additionally calculated on the upper half of each sequence.

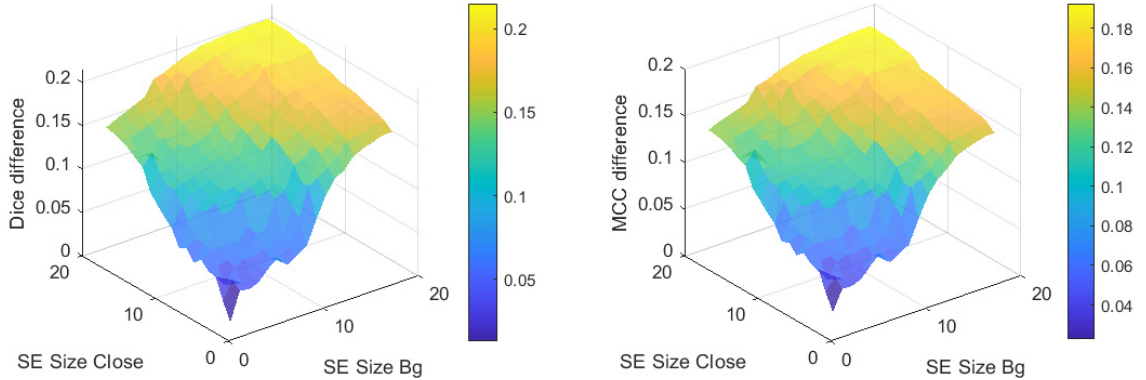
All four sequences are used to evaluate the effect of the parameters. Because two parameters are optimized, the generically denoted score  $S$  for the segmentation of the whole sequence is calculated as  $S_{i,j}$  for  $i, j \in \{1, \dots, 18\}$  [px].  $i$  denotes the SE size  $SE_{Close}$  for the morphological closing of the mask and  $j$  denotes the SE size  $SE_{Bg}$  for the morphological background removal. For further details, see also section 3.4.1. All slices are scaled to a size of  $256 \times 256$  pixels. The corresponding score for the upper half of the sequence is denoted as  $S'$ .

Figure 4.5 shows exemplary results for the different selection of parameters  $SE_{Close}$  and  $SE_{Bg}$  applied to sequence 03. See also figures B.9, B.10, and B.11 for results of other sequences.

## 4. Results



**(a)** Dice score and MCC score for each pairwise selection of the foreground segmentation parameters. Top row: Scores calculated on the whole the sequence. Bottom row: Scores calculated on the upper half of the sequence.



**(b)** Difference between the scores calculated on the whole sequence and calculated on the upper half of the sequence for each metric.

**Figure 4.5.:** Results for the pairwise selection of the foreground segmentation of sequence 03 with brain ground truth as brain segmentation.

Figure 4.5a shows that the scores for the upper half of the sequence form a plateau, while the scores for the whole sequence form a distinct peak. The difference between the scores for the upper half of the sequence and the whole sequence is not significantly high for small  $i, j$  (figure 4.5b). This is similar to the scores of the other sequences. The idea to find optimal parameters is to find a compromise where the loss of score for the skullcap is insignificantly lower, while the score for the entire skull is significantly improved.

The optimization uses the MCC score as the decisive metric because it is the most robust and reliable out of the two metrics. To determine the best parameters that lead to a reasonable result on all sequences, a common trend of the results which depend on the selection of  $SE_{Close}$  and  $SE_{Bg}$  is identified. Based on this trend a maximum average MCC score is calculated and the corresponding SE sizes are chosen to be the default values of the foreground segmentation.

In order to check if a common trend of the score matrices  $MCC$  and  $MCC'$  is present, the correlation coefficients between the MCC score matrices of all sequences must be studied. This includes the correlation between the MCC scores for the upper half of the sequence and the whole sequence. The correlation coefficient of two matrices is calculated as

$$\rho_{A,B} = \frac{\sum_i \sum_j (A_{i,j} - \hat{A}) \cdot (B_{i,j} - \hat{B})}{\sqrt{(\sum_i \sum_j (A_{i,j} - \hat{A})^2) \cdot (\sum_i \sum_j (B_{i,j} - \hat{B})^2)}}, \quad (4.10)$$

where  $A, B \in \mathbb{R}^2$ ,  $\hat{A}$  mean of  $A$  and  $\hat{B}$  mean of  $B$ .<sup>2</sup>  $\rho_{A,B} = \rho_{B,A}$  applies.  $MCC_k$  represents the MCC score results for the whole sequence  $k$ , where

$$k = \begin{cases} 1, & \text{for sequence 03} \\ 2, & \text{for sequence 04} \\ 3, & \text{for sequence ZI} \\ 4, & \text{for sequence ME} \end{cases} . \quad (4.11)$$

$MCC'_k$  is the respective MCC score matrix for the upper half of the sequence.

---

<sup>2</sup>Adapted from [https://de.mathworks.com/help/images/ref/corr2.html?s\\_tid=doc\\_ta](https://de.mathworks.com/help/images/ref/corr2.html?s_tid=doc_ta), accessed 2021-04-25.

#### 4. Results

---

$$\mathbf{C}_w = \begin{matrix} & \begin{matrix} MCC_1 & MCC_2 & MCC_3 & MCC_4 \end{matrix} \\ \begin{matrix} MCC_1 \\ MCC_2 \\ MCC_3 \\ MCC_4 \end{matrix} & \begin{pmatrix} 1 & 0.8679 & 0.9007 & 0.5191 \\ 0.8679 & 1 & 0.8704 & 0.4120 \\ 0.9007 & 0.8704 & 1 & 0.6870 \\ 0.5191 & 0.4120 & 0.6870 & 1 \end{pmatrix} \end{matrix}$$

**(a)** Pairwise correlation coefficients for the MCC score matrices of the evaluation on the whole sequences.

$$\mathbf{C}_u = \begin{matrix} & \begin{matrix} MCC'_1 & MCC'_2 & MCC'_3 & MCC'_4 \end{matrix} \\ \begin{matrix} MCC'_1 \\ MCC'_2 \\ MCC'_3 \\ MCC'_4 \end{matrix} & \begin{pmatrix} 1 & 0.9596 & 0.7960 & 0.6961 \\ 0.9596 & 1 & 0.7874 & 0.6481 \\ 0.7960 & 0.7874 & 1 & 0.3623 \\ 0.6961 & 0.6481 & 0.3623 & 1 \end{pmatrix} \end{matrix}$$

**(b)** Pairwise correlation coefficients for the MCC score matrices of the evaluation on the upper half of each sequence.

$$\mathbf{C}_i = \begin{matrix} & \begin{matrix} MCC'_1 & MCC'_2 & MCC'_3 & MCC'_4 \end{matrix} \\ \begin{matrix} MCC_1 \\ MCC_2 \\ MCC_3 \\ MCC_4 \end{matrix} & \begin{pmatrix} 0.6400 & 0.5693 & 0.8478 & 0.2328 \\ 0.5693 & 0.4965 & 0.8165 & 0.0276 \\ 0.8478 & 0.8165 & 0.8804 & 0.0565 \\ 0.2328 & 0.0276 & 0.0565 & 0.2733 \end{pmatrix} \end{matrix}$$

**(c)** Pairwise correlation coefficients for the MCC score matrices of the evaluation on the upper half of each sequence and the evaluation on the whole sequence.

**Figure 4.6.:** Pairwise correlation coefficients for the different MCC score matrices of all sequences.

Figure 4.6 shows a strong correlation between the MCC scores for sequences 1 – 3, but the MCC scores of sequence 4 are weakly correlated with the other results. The pixel spacing of each slice in sequences 1 – 3 is 0.0781 mm, whereas it is 0.0861 mm for slices in sequence 4. Sequence 4 is an older sequence used to test the robustness for different parameters of the MRI acquisition from the parameters used in the HEiKA framework. It is evident that further improvement in terms of robustness is needed in the future. Nevertheless, this thesis focuses on the characteristics of the MR images within the HEiKA project in order to find an accurate solution for them. As a consequence, the optimization does not take into account sequence 4 for a representative optimization result.

The optimization is based on the detection of the maximum average MCC score. For each selection of  $i, j \in \{1, \dots, 18\}$  and  $k \in \{1, 2, 3\}$ , the entry  $\tilde{W}_{i,j}$  of matrix  $\tilde{W}$  is representing the average  $MCC_{k_{i,j}}$  score, the entry  $\tilde{U}_{i,j}$  of matrix  $\tilde{U}$  is representing the average  $MCC'_{k_{i,j}}$  score, and the entry  $\tilde{A}_{i,j}$  of matrix  $\tilde{A}$  is representing the average of  $\tilde{W}_{i,j}$  and  $\tilde{U}_{i,j}$  (eq. 4.12).  $\tilde{W}$  and  $\tilde{U}$  are weighted equally. The matrix  $\tilde{A}$  gives information about the best compromising selection of  $i, j$  for sequences 1 – 3.

$$\tilde{W} = \frac{1}{3} \cdot \sum_{k=1}^3 MCC_k, \quad \tilde{U} = \frac{1}{3} \cdot \sum_{k=1}^3 MCC'_k, \quad \tilde{A} = \frac{1}{2} \cdot (\tilde{W} + \tilde{U}). \quad (4.12)$$

$$\tilde{\mathbf{C}}_{avg} = \begin{pmatrix} \tilde{W} & \tilde{U} & \tilde{A} \\ \tilde{W} & 1 & 0.6846 & 0.9271 \\ \tilde{U} & 0.6846 & 1 & 0.9079 \\ \tilde{A} & 0.9271 & 0.9079 & 1 \end{pmatrix}$$

**Figure 4.7.:** Pairwise correlation coefficients for  $\tilde{W}$ ,  $\tilde{U}$ , and  $\tilde{A}$ .

$$\begin{aligned} \rho_{\tilde{A},MCC_1} &= 0.9216, & \rho_{\tilde{A},MCC_2} &= 0.8594, \\ \rho_{\tilde{A},MCC_3} &= 0.8823, & \rho_{\tilde{A},MCC_4} &= 0.5522, \\ \rho_{\tilde{A},MCC'_1} &= 0.8298, & \rho_{\tilde{A},MCC'_2} &= 0.8073, \\ \rho_{\tilde{A},MCC'_3} &= 0.9700, & \rho_{\tilde{A},MCC'_4} &= 0.3821. \end{aligned} \tag{4.13}$$

Equation 4.13 shows that  $\tilde{A}$  is strongly correlated to the MCC score matrices of sequences 1 – 3 and still weakly correlated with the MCC score matrices of sequence 4. In order to find a reasonable selection of the parameters, the maximum value  $v_{max}$  of  $\tilde{A}$  is calculated. The result is

$$v_{max} = \max_{i,j} \tilde{A}_{i,j} = 0.7529, \tag{4.14}$$

for  $i = 2$  and  $j = 5$ . This translates to a SE size of 2 pixels for  $SE_{Close}$  and a SE size of 5 pixels for  $SE_{Bg}$ . Because the optimization is focused on sequences 1 – 3, the pixel values are converted into millimeters with a pixel spacing of 0.0781 mm in order to generalize the SE size for MRI sequences with different resolutions:

$$\begin{aligned} 2 \cdot 0.0781 &= 0.1562 \quad [px * mm], \\ 5 \cdot 0.0781 &= 0.3905 \quad [px * mm]. \end{aligned} \tag{4.15}$$

AuSoMS uses the pixel spacing of the input data to convert these values into pixels.

## 4.4. Evaluation of the entire automatic segmentation

The preceding sections define the optimal parameters for the entire skull segmentation. Now the evaluation of the results of a fully automatic segmentation can be completed. Figure 4.8 shows an exemplary result for the automatic skull segmentation.

Because of the random component in the brain segmentation, the evaluation procedure is analogous to the brain segmentation study in section 4.2. Each sequence is segmented and evaluated 1000 times. The box plots 4.10, 4.11, and 4.12 were created with the same parameters as in section 4.2.

For this evaluation, all slices were scaled to  $256 \times 256$  pixels. Spot evaluations for a slice size of  $512 \times 512$  pixels showed no significant change in scores. The pixel spacing was adjusted when scaling the slices to ensure consistent behavior of AuSoMS. AuSoMS

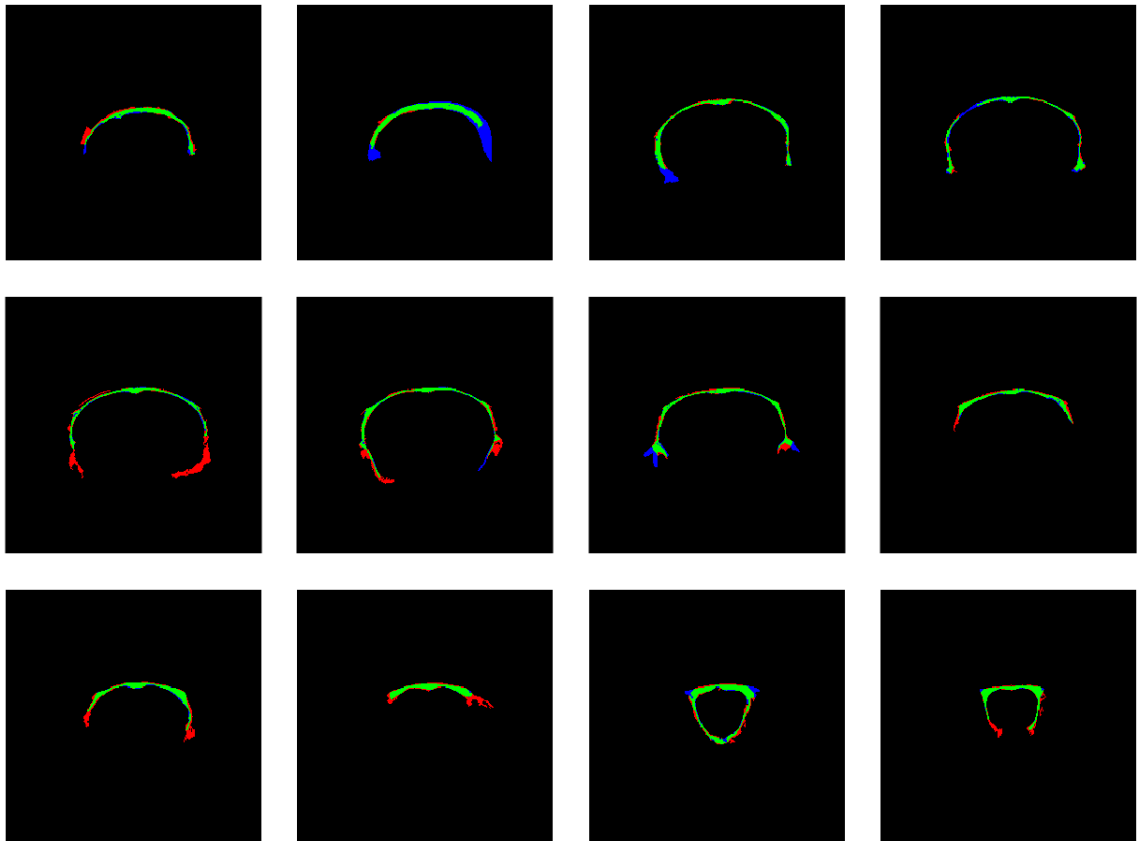
#### 4. Results

---

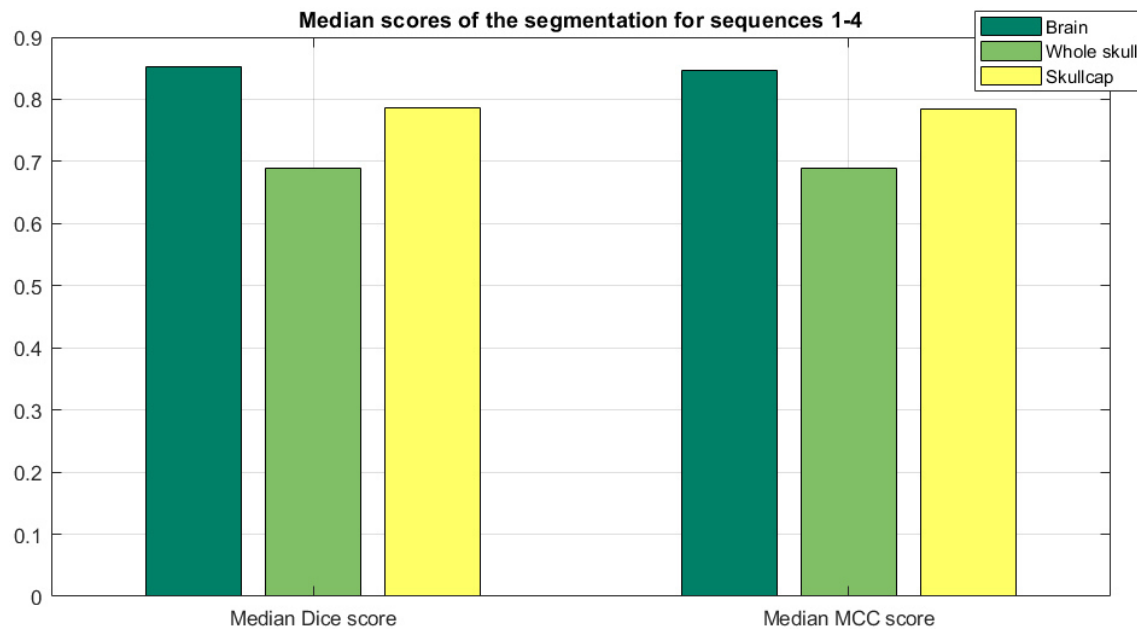
uses the pixel spacing and the slice thickness to convert the default parameters specified in the code from millimeters to pixels.

Figure 4.8 shows that AuSoMS recognizes the overall location of the skull segment correctly. There is neither severe overestimation nor underestimation of the skullcap visible. Figures B.12 and B.13 show exemplary outputs for sequences *04* and *ZI*. AuSoMS also achieves a reasonable result for these sequences. The median MCC score is 0.8467 for the brain segmentation, 0.69 for the overall segmentation and 0.7844 for the segmentation of the skullcap. The corresponding median Dice scores are nearly identical (figure 4.9). As expected, the random component of the brain segmentation is reflected in the overall results (figure 4.10, figure 4.11, and figure 4.12).

However, the result for sequence *ME* is particularly striking. Although the brain segmentation achieves rather good scores for this sequence, the skull segmentation does perform significantly better on the other sequences. This outcome can be due to the high amount of noise in sequence *ME*. If this should be the case for future MRI sequences in the HEiKA project, it could be necessary to further optimize the parameters and increase the overall robustness of AuSoMS.



**Figure 4.8:** Exemplary output of the automatic skull segmentation for sequence *03*.  
Green: True positives *TP*, Red: False positives *FP*, Black: True negatives *TN*, Blue: False negatives *FN*.



**Figure 4.9.:** Median scores for brain segmentation, skull segmentation on the whole sequence, and segmentation of the skullcap (upper half of skull segmentation).

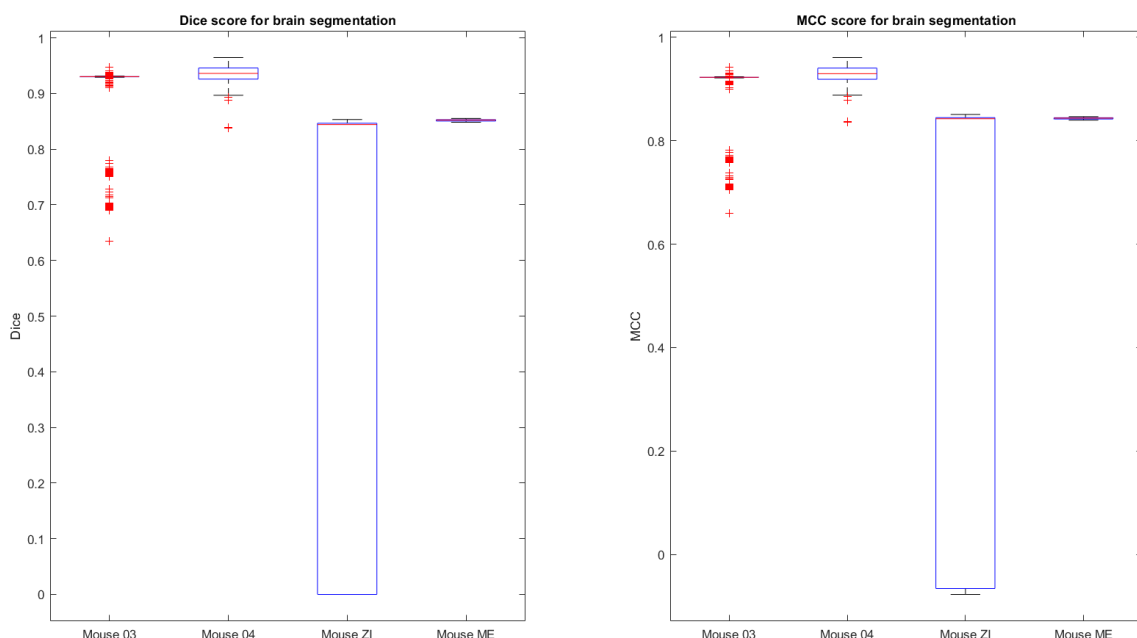


**Figure 4.10.:** Dice score and MCC score for the brain segmentation of all 4 sequences and 1000 repetitions per sequence.

## 4. Results

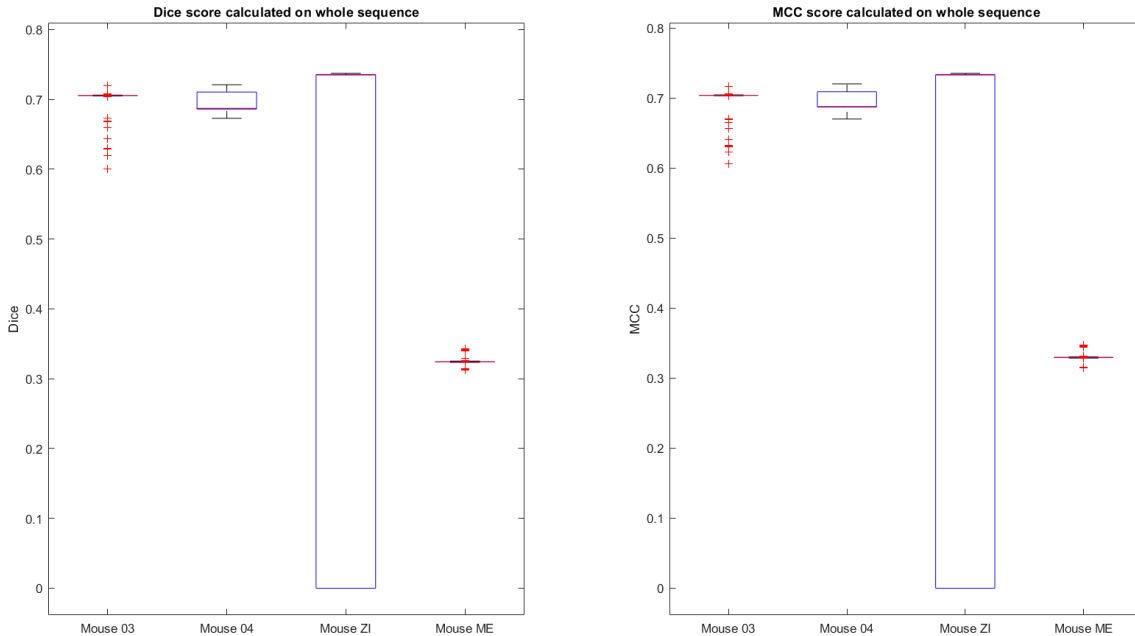


**Figure 4.11.:** Results for the skull segmentation on whole sequence of all 4 sequences and 1000 repetitions per sequence.

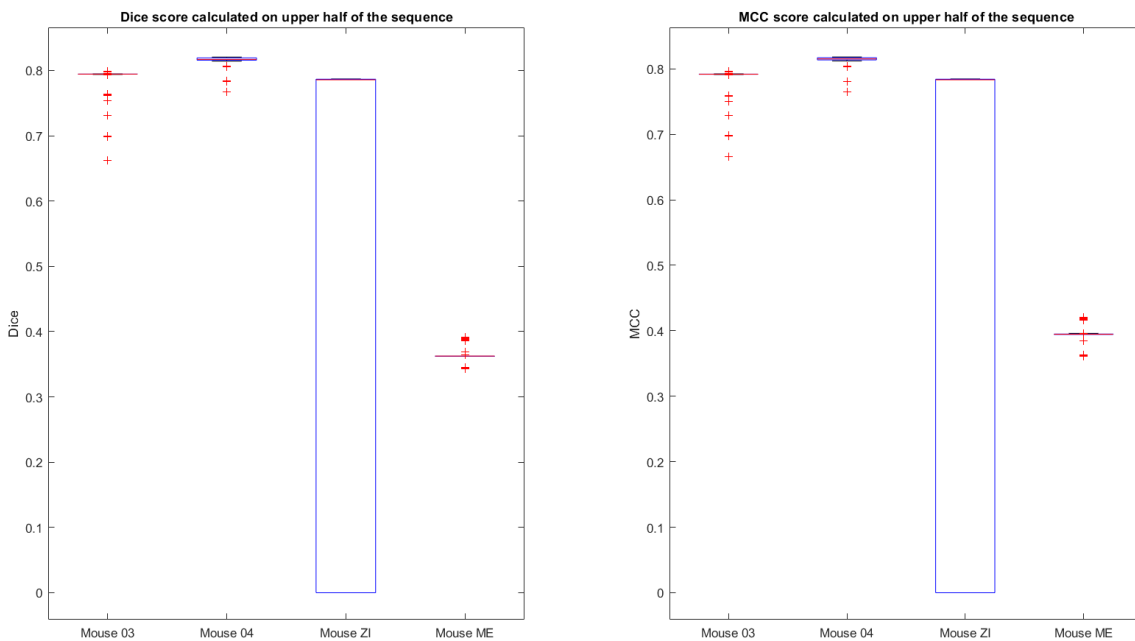


**Figure 4.12.:** Results for the skull segmentation on the upper half of all 4 sequences and 1000 repetitions per sequence.

## 4.5. Performance

AuSoMS is able to segment the available data in just a few seconds. Table 4.1 shows the computation times for different slice resolutions. The times were measured on a system with an 8-core Intel(R) Core(TM) i7-9700K CPU @3.60 GHz and a 32GB DDR4 RAM @2666 MHz running Windows 10. AuSoMS is implemented in MATLAB version

R2020b and utilizes only the CPU. To accelerate the segmentation further, code using graphic processing unit acceleration could be used in future.

The 3D-PCNN method is a potential bottleneck. For isometric volumes the computation time can reach up to 48 minutes [7]. However, in this project the sequences are limited to a low amount of slices, a large slice thickness, and ample spacing between slices. This limitation allows for faster brain segmentation with the 3D-PCNN method.

Bias field correction with MICO and the pre-processing - especially the denoising with NLMF - are the most computationally intensive methods of the remaining methods (table 4.2). The computation time of the NLMF method increases, because with higher resolution and the same search radius in mm, the search distance in pixels increases.

Three parts of AuSoMS are parallelized using the MATLAB parallel processing toolbox. Pre-processing, the creation of the ROI around the brain masks and the assessment of segments based on their maximum Feret diameter are executed for each slice in parallel.

**Table 4.1.:** Exemplary segmentation computation times using a single 3D-PCNN brain segmentation.

Sequence	3D-PCNN [s]	Remaining methods [s]	Resolution [px × px]	Slices
03	4.855	1.395	256 × 256	12
	29.277	9.937	512 × 512	12
04	5.025	1.255	256 × 256	12
	28.224	10.024	512 × 512	12
ZI	8.265	1.395	256 × 256	25
	43.386	20.121	512 × 512	25
ME	6.163	0.843	256 × 256	8
	70.954	5.528	512 × 512	8

**Table 4.2.:** Exemplary computation times of pre-processing and bias field correction.

Sequence	Pre-processing [s]	Bias field correction [s]	Resolution [px × px]	Slices
03	0.292	0.835	256 × 256	12
	5.243	4.322	512 × 512	12
04	0.290	0.777	256 × 256	12
	5.148	4.305	512 × 512	12
ZI	0.582	1.821	256 × 256	25
	10.335	8.973	512 × 512	25
ME	0.176	0.516	256 × 256	8
	2.303	2.884	512 × 512	8

# 5. Summary, Discussion and Conclusion

This thesis addresses the challenge of segmenting the skull in MRI images of mice automatically. The proposed method called AuSoMS enables the segmentation of rodent MRI slices acquired in the transversal plane without manual intervention.

AuSoMS pre-processes the input sequence using histogram equalization with CLAHE, contrast enhancement, and denoising with NLMF. The stack of pre-processed slices is then passed to two different segmentations. The foreground segmentation identifies the dark structures of the mouse head in each MRI slice. The brain segmentation performs a volume-based segmentation of the brain in the pre-processed stack using the 3D-PCNN algorithm. The SE sizes for the morphological operations of foreground segmentation and brain segmentation are statistically optimized. The skull segmentation combines the results of these two segmentations to locate the dark structures of the head in the proximity of the brain based on the empirical maximum skull thickness. Furthermore, the segments are assessed based on their maximum Feret diameter to filter out small fragments of the segmentation. The spatial information of neighboring slices aids the identification and removal of large segments not depicting the skull. In many slices, the skull still consists of two segments after the skull segmentation. AuSoMS introduces an algorithm to close the gap between the two segments if the size of the gap does not exceed an empirically chosen width.

This thesis introduces a new approach to segment the skull in rodent cranial MRI scans automatically. To our knowledge, this approach is also the first suggestion on that topic. The implementation can cope with sparse data and is relatively accurate, achieving a Matthews Correlation Coefficient score of approximately 0.8 for the skullcap. The approach combines multiple well-established image processing methods, empirical knowledge, and spatial information without the need for a vast amount of labeled data.

The random component of the brain segmentation can lead to a high variance in the results, especially for sequence *ZI*. The behavior of the brain segmentation for more than 1000 repetitions still has to be studied. Because of time constraints, the introduced method aiming to reduce the variance was performed with 10 repetitions of the 3D-PCNN segmentation for each repetition of the brain segmentation. Extending this number could enable the reduction of the variance in the future. In the original paper introducing the 3D-PCNN method, the brain segmentation is more accurate. The discrepancy of the brain segmentation results could be due to the large slice thickness, accompanying distorted voxel dimensions, and movement artifacts or PVE artifacts. The artifacts may be different in the MR images acquired in the HEiKA project.

As an alternative, other approaches for brain segmentation in rodent cranial MRI scans could be incorporated or implemented and compared with the 3D-PCNN algorithm in terms of robustness and computation time.

The evaluation of the segmentation for sequence *ME* shows that the skull segmentation is sensitive to noise in the MR image. However, future pre-sonication scans in the HEiKA project most likely resemble characteristics as can be observed in sequences *03* and *04*. The variance of the brain segmentation was not as high for these sequences as for sequence *ZI*. There is less noise in sequences *03*, *04*, and *ZI* than in sequence *ME*. The skullcap can be adequately extracted in most cases. In the future, the approach could be optimized regarding the performance with noisy images.

The 3D-PCNN algorithm is less robust for T1 weighted images than for T2 weighted images [7]. Therefore, T2 weighted images should be used for the segmentation with AuSoMS.

Post-processing is able to approximate the skull in small gaps. However, AuSoMS does not consider the overall curvature of the skull during the approximation of the skull in the gaps. AuSoMS does not correct the skull in case wide gaps are present between two segments. If the skull segment is divided into more than two segments, AuSoMS could be extended to close small gaps between multiple segments. Wang and Zhang [38] propose an algorithm that uses the geodesic distance and neighborhood information to link edges. This algorithm is a potential starting point for solving the problem involving artifacts.

The parameters are optimized for the data available and rely on empirical knowledge. It remains to show how AuSoMS behaves on other datasets. Further evaluation requires a more extensive set of data along with its ground truth. Because there is only few labeled data available, AuSoMS does not use prevalent neural networks like U-Net. With more labeled data at hand, a deep neural network could be trained. It would be interesting to see how the network handles the artifacts. Explainable artificial intelligence in medical image processing could help overcome the "black box" issue [35]. The new approach could be combined with explainable artificial intelligence to comprehend the detection of skull bone tissue for occurring artifacts. The observations could be used to improve AuSoMS.

AuSoMS can segment MRI sequences with a slice resolution of  $256 \times 256$  pixels in a couple of seconds. The runtime is sufficient for the foreseen usage in automated sonication optimization. The small number of slices per sequence favors the processing time. Although some methods are parallelized, AuSoMS only uses the CPU. The generation and usage of accelerated code on graphic processing units could further improve the processing time.

The approach proposed in this work fills a gap in research on automatic segmentation of the skull in MRI images and can segment the mouse skull in conventional T2 weighted MRI images without manual intervention. The development of the approach in MATLAB considered the framework of the HEiKA project.

The implementation of AuSoMS enables the automatic optimization of the FUS parameters without requiring additional adjustments of the BBB opening protocol, making this thesis an important part of the HEiKA project. Furthermore, the segmentation provides for automatic brain segmentation, which can be used for the FUS sonication simulations. There could be more methods suggesting automatic skull segmentation in rodent cranial MRI scans in the future. As the first solution for this challenge, AuSoMS represents a reference point for the performance of future methods.

# Bibliography

- [1] 2020 Alzheimer's disease facts and figures. *Alzheimer's & Dementia*, 16(3):391–460, 2020. doi: 10.1002/alz.12068.
- [2] Horst Bickel. Die Häufigkeit von Demenzerkrankungen: Informationsblatt 1, 2020. URL [https://www.deutsche-alzheimer.de/fileadmin/alz/pdf/factsheets/infoblatt1\\_haeufigkeit\\_demenzerkrankungen\\_dalzg.pdf](https://www.deutsche-alzheimer.de/fileadmin/alz/pdf/factsheets/infoblatt1_haeufigkeit_demenzerkrankungen_dalzg.pdf). Accessed 2021-04-06.
- [3] Derek Bradley and Gerhard Roth. Adaptive Thresholding using the Integral Image. *Journal of Graphics Tools*, 12(2):13–21, 2007. ISSN 1086-7651. doi: 10.1080/2151237X.2007.10129236.
- [4] A. Buades, B. Coll, and J.-M. Morel. A Non-Local Algorithm for Image Denoising. In *2005 IEEE Computer Society Conference on Computer Vision and Pattern Recognition (CVPR'05)*, volume 2, pages 60–65 vol. 2, 2005. ISBN 0-7695-2372-2. doi: 10.1109/CVPR.2005.38.
- [5] Carlos E. Cardenas, Jinzhong Yang, Brian M. Anderson, Laurence E. Court, and Kristy B. Brock. Advances in Auto-Segmentation. *Seminars in Radiation Oncology*, 29(3):185–197, 2019. ISSN 1532-9461. doi: 10.1016/j.semradonc.2019.02.001.
- [6] Davide Chicco and Giuseppe Jurman. The advantages of the Matthews correlation coefficient (MCC) over F1 score and accuracy in binary classification evaluation. *BMC Genomics*, 21(1):6, 2020. doi: 10.1186/s12864-019-6413-7.
- [7] Nigel Chou, Jiarong Wu, Jordan Bai Bingren, Anqi Qiu, and Kai-Hsiang Chuang. Robust Automatic Rodent Brain Extraction Using 3-D Pulse-Coupled Neural Networks (PCNN). *IEEE Transactions on Image Processing*, 20(9):2554–2564, 2011. ISSN 1941-0042. doi: 10.1109/TIP.2011.2126587.
- [8] Margaret J. Cook. The Anatomy of the Laboratory Mouse, 1965. URL <http://www.informatics.jax.org/cookbook/>. Adapted for Web by Mouse Genome Informatics, Bar Harbor, Maine, April 2005, Revised February 2008. Accessed 2021-04-08.
- [9] Leon Derczynski. Complementarity, F-score, and NLP Evaluation. In Nicoletta Calzolari (Conference Chair), Khalid Choukri, Thierry Declerck, Sara Goggi, Marko Grobelnik, Bente Maegaard, Joseph Mariani, Helene Mazo, Asuncion Moreno, Jan Odijk, and Stelios Piperidis, editors, *Proceedings of the Tenth International Conference on Language Resources and Evaluation (LREC 2016)*, Paris, France, may 2016. European Language Resources Association (ELRA). ISBN 978-2-9517408-9-1.
- [10] Wei Li Ding, Feng Jiang, and Jia Qing Yan. Automatic Segmentation of the Skull in MRI Sequences Using Level Set Method. *Applied Mechanics and Materials*, 58-60: 2370–2375, 2011. doi: 10.4028/www.scientific.net/AMM.58-60.2370.

- [11] Belma Dogdas, David W. Shattuck, and Richard M. Leahy. Segmentation of skull and scalp in 3-D human MRI using mathematical morphology. *Human Brain Mapping*, 26(4):273–285, 2005. ISSN 1065-9471. doi: 10.1002/hbm.20159.
- [12] Max Dünnwald, Matthew J. Betts, Alessandro Sciarra, Emrah Düzel, and Steffen Oeltze-Jafra. Automated Segmentation of the Locus Coeruleus from Neuromelanin-Sensitive 3T MRI Using Deep Convolutional Neural Networks. In Thomas Tolxdorff, Thomas M. Deserno, Heinz Handels, Andreas Maier, Klaus H. Maier-Hein, and Christoph Palm, editors, *Bildverarbeitung für die Medizin 2020*, Informatik aktuell, pages 61–66. Springer Fachmedien Wiesbaden, Wiesbaden, 2020. ISBN 978-3-658-29266-9. doi: 10.1007/978-3-658-29267-6\_13.
- [13] Bradley J. Erickson, Panagiotis Korfiatis, Zeynettin Akkus, and Timothy L. Kline. Machine Learning for Medical Imaging. *Radiographics : a review publication of the Radiological Society of North America, Inc*, 37(2):505–515, 2017. doi: 10.1148/rg.2017160130.
- [14] Riccardo Feo and Federico Giove. Towards an efficient segmentation of small rodents brain: A short critical review. *Journal of Neuroscience Methods*, 323:82–89, 2019. doi: 10.1016/j.jneumeth.2019.05.003.
- [15] Leila Ghanbari, Mathew L. Rynes, Jia Hu, Daniel S. Schulman, Gregory W. Johnson, Michael Laroque, Gabriella M. Shull, and Suhasa B. Kodandaramaiah. Principles of Computer Numerical Controlled Machining Applied to Cranial Microsurgery. *Scientific reports*, 9(1):1023, 2019. doi: 10.1038/s41598-018-37073-w.
- [16] Maryellen L. Giger. Machine Learning in Medical Imaging. *Journal of the American College of Radiology : JACR*, 15(3 Pt B):512–520, 2018. doi: 10.1016/j.jacr.2017.12.028.
- [17] Abhijit Guha Roy, Sailesh Conjeti, Nassir Navab, and Christian Wachinger. Quick-NAT: A fully convolutional network for quick and accurate segmentation of neuroanatomy. *NeuroImage*, 186:713–727, 2019. ISSN 1053-8119. doi: 10.1016/j.neuroimage.2018.11.042.
- [18] Paul S. Heckbert, editor. *Graphics Gems*, volume 4 of *Graphics Gems*. AP Professional, Boston, 1994. ISBN 9780123361561.
- [19] Li-Ming Hsu, Shuai Wang, Paridhi Ranadive, Woomi Ban, Tzu-Hao Harry Chao, Sheng Song, Domenic Hayden Cerri, Lindsay R. Walton, Margaret A. Broadwater, Sung-Ho Lee, Dinggang Shen, and Yen-Yu Ian Shih. Automatic Skull Stripping of Rat and Mouse Brain MRI Data Using U-Net. *Frontiers in neuroscience*, 14:568614, 2020. ISSN 1662-4548. doi: 10.3389/fnins.2020.568614.
- [20] V. Koo, P. W. Hamilton, and K. Williamson. Non-invasive in vivo Imaging in Small Animal Research. *Cellular oncology : the official journal of the International Society for Cellular Oncology*, 28(4):127–139, 2006. ISSN 1570-5870. doi: 10.1155/2006/245619.
- [21] Chunming Li, John C. Gore, and Christos Davatzikos. Multiplicative intrinsic component optimization (MICO) for MRI bias field estimation and tissue segmentation. *Magnetic Resonance Imaging*, 32(7):913–923, 2014. ISSN 0730-725X. doi: 10.1016/j.mri.2014.03.010.

- [22] Jinxiang Ma, Xinnan Fan, Simon X. Yang, Xuewu Zhang, and Xifang Zhu. Contrast Limited Adaptive Histogram Equalization Based Fusion for Underwater Image Enhancement. *International Journal of Pattern Recognition and Artificial Intelligence*, 32(07):1854018, 2018. ISSN 0218-0014. doi: 10.1142/S0218001418540186.
- [23] Miguel Ángel González Ballester, Andrew P. Zisserman, and Michael Brady. Estimation of the partial volume effect in MRI. *Medical Image Analysis*, 6(4):389–405, 2002. ISSN 1361-8415. doi: 10.1016/S1361-8415(02)00061-0.
- [24] Murali Murugavel and John M. Sullivan. Automatic cropping of MRI rat brain volumes using pulse coupled neural networks. *NeuroImage*, 45(3):845–854, 2009. doi: 10.1016/j.neuroimage.2008.12.021.
- [25] Jesper D. Nielsen, Kristoffer H. Madsen, Oula Puonti, Hartwig R. Siebner, Christian Bauer, Camilla Gøbel Madsen, Guilherme B. Saturnino, and Axel Thielscher. Automatic skull segmentation from MR images for realistic volume conductor models of the head: Assessment of the state-of-the-art. *NeuroImage*, 174:587–598, 2018. doi: 10.1016/j.neuroimage.2018.03.001.
- [26] Alfred Nischwitz, Max Fischer, Peter Haberäcker, and Gudrun Socher. *Bildverarbeitung*. Springer Fachmedien Wiesbaden, Wiesbaden, 2020. ISBN 978-3-658-28704-7. doi: 10.1007/978-3-658-28705-4.
- [27] Ipek Oguz, Honghai Zhang, Ashley Rumple, and Milan Sonka. RATS: Rapid Automatic Tissue Segmentation in rodent brain MRI. *Journal of Neuroscience Methods*, 221:175–182, 2014. doi: 10.1016/j.jneumeth.2013.09.021.
- [28] Nobuyuki Otsu. A Threshold Selection Method from Gray-Level Histograms. *IEEE Transactions on Systems, Man, and Cybernetics*, 9(1):62–66, 1979. ISSN 0018-9472. doi: 10.1109/TSMC.1979.4310076.
- [29] M. Pechaud, M. Jenkinson, and S. Smith. BET2 - MRI-Based Estimation of Brain, Skull and Scalp Surfaces FMRIB Technical Report TR06MP1. Report XXXIII. *BET2-MRI-Based Estimation of Brain, Skull and Scalp Surfaces, Technical report, FMRIB Technical Report TR06MP1*, pages 81–87, 2006.
- [30] Oleg S. Pianykh. *Digital Imaging and Communications in Medicine (DICOM)*. Springer Berlin Heidelberg, Berlin, Heidelberg, 2008. ISBN 978-3-540-74570-9. doi: 10.1007/978-3-540-74571-6.
- [31] Olaf Ronneberger, Philipp Fischer, and Thomas Brox. U-Net: Convolutional Networks for Biomedical Image Segmentation. In Nassir Navab, Joachim Hornegger, William M. Wells, and Alejandro F. Frangi, editors, *Medical Image Computing and Computer-Assisted Intervention – MICCAI 2015*, pages 234–241, Cham, 2015. Springer International Publishing. ISBN 978-3-319-24574-4.
- [32] Nicole Ruiter and Marc Fatar. Magnetic resonance-guided opening of the blood-brain barrier using focused ultrasound for cell-mediated therapies of brain diseases. WebPage, 2020. URL <https://www.heika-research.de/en/research/medical-technology-health-mth/magnetic-resonance-guided-opening-blood-brain-barrier-using>. Accessed 2021-04-05.

- [33] Himanshu Singh and Vivek Singh. A Comparative Analysis on Histogram Equalization Techniques for Medical Image Enhancement. *International Journal of Advanced Research in Computer Science and Software Engineering*, 7(6):364–370, 2017. ISSN 22776451. doi: 10.23956/ijarcsse/V7I6/0269.
- [34] Vanessa K. Tidwell, Joong H. Kim, Sheng-Kwei Song, and Arye Nehorai. Automatic segmentation of rodent spinal cord diffusion MR images. *Magnetic Resonance in Medicine*, 64(3):893–901, 2010. doi: 10.1002/mrm.22416.
- [35] Erico Tjoa and Cuntai Guan. A Survey on Explainable Artificial Intelligence (XAI): Toward Medical XAI. *IEEE Transactions on Neural Networks and Learning Systems*, PP, 2020. doi: 10.1109/TNNLS.2020.3027314.
- [36] Thomas Tolxdorff, Thomas M. Deserno, Heinz Handels, Andreas Maier, Klaus H. Maier-Hein, and Christoph Palm. *Bildverarbeitung für die Medizin 2020*. Springer Fachmedien Wiesbaden, Wiesbaden, 2020. ISBN 978-3-658-29266-9. doi: 10.1007/978-3-658-29267-6.
- [37] Defeng Wang, Lin Shi, Winnie C. W. Chu, Jack C. Y. Cheng, and Pheng Ann Heng. Segmentation of human skull in MRI using statistical shape information from CT data. *Journal of Magnetic Resonance Imaging : JMRI*, 30(3):490–498, 2009. ISSN 1053-1807. doi: 10.1002/jmri.21864.
- [38] Zhipeng Wang and Hong Zhang. Edge linking using geodesic distance and neighborhood information. In *IEEE*, pages 151–155. IEEE / Institute of Electrical and Electronics Engineers Incorporated, 2008. ISBN 978-1-4244-2494-8. doi: 10.1109/AM.2008.4601650.
- [39] Vitalis Wiens. Volumetric Segmentation of Complex Bone Structures from Medical Imaging Data Using Reeb Graphs. *Proceedings of CESCG 2013 – The 17th Central European Seminar on Computer Graphics*, pages 113–120, 2013. (non-peer-reviewed).
- [40] Xiaofeng Yang and Baowei Fei. Multiscale segmentation of the skull in MR images for MRI-based attenuation correction of combined MR/PET. *Journal of the American Medical Informatics Association : JAMIA*, pages 1037–1045, 2013. doi: 10.1136/amiajnl-2012-001544.
- [41] A. P. Zijdenbos, B. M. Dawant, R. A. Margolin, and A. C. Palmer. Morphometric analysis of white matter lesions in MR images: method and validation. *IEEE Transactions on Medical Imaging*, 13(4):716–724, 1994. ISSN 0278-0062. doi: 10.1109/42.363096.
- [42] Karel Zuiderveld. Contrast Limited Adaptive Histogram Equalization. In Paul S. Heckbert, editor, *Graphics Gems*, Graphics Gems, pages 474–485. AP Professional, Boston, 1994. ISBN 9780123361561. doi: 10.1016/B978-0-12-336156-1.50061-6.

# Appendix

## A. Algorithms

---

**Algorithm 2** Outlier correction

---

**Require:**  $N \geq 2$

```
1: for  $n = 1, \dots, N$  do
2:   if  $n = 1$  then
3:      $current \leftarrow \tilde{F}_{roi,n}$ 
4:      $next \leftarrow \tilde{F}_{roi,n+1}$ 
5:      $distNext \leftarrow \text{BWDISTGEODESIC}(current, next)$ 
6:      $D \leftarrow distNext == Inf$ 
7:   else if  $n = N$  then
8:      $current \leftarrow \tilde{F}_{roi,n}$ 
9:      $last \leftarrow \tilde{F}_{roi,n-1}$ 
10:     $distLast \leftarrow \text{BWDISTGEODESIC}(current, last)$ 
11:     $D \leftarrow distNext == Inf$ 
12:   else
13:      $last \leftarrow \tilde{F}_{roi,n-1}$ 
14:      $current \leftarrow \tilde{F}_{roi,n}$ 
15:      $next \leftarrow \tilde{F}_{roi,n+1}$ 
16:      $distLast \leftarrow \text{BWDISTGEODESIC}(current, last)$ 
17:      $distNext \leftarrow \text{BWDISTGEODESIC}(current, next)$ 
18:      $D \leftarrow (distLast == Inf) \wedge (distNext == Inf)$ 
19:   end if
20:    $\tilde{F}_{roi,n} \leftarrow \tilde{F}_{roi,n} \wedge \neg D$ 
21: end for
```

---

---

**Algorithm 3** Post-processing

---

**Require:**  $t, g \in \mathbb{R}$

```

1: for  $n = 1, \dots, N$  do
2:    $S \leftarrow \tilde{F}_{roi,n}$ 
3:    $numObjects \leftarrow \text{BICONNCOMP}(S)$ 
4:   if  $numObjects = 2$  then
5:      $s1 \leftarrow$  image only containing first segment
6:      $s2 \leftarrow$  image only containing second segment
7:      $d1 \leftarrow \text{BWDIST}(s1)$ 
8:      $d2 \leftarrow \text{BWDIST}(s2)$ 
9:      $D \leftarrow d1 + d2$ 
10:     $minDist \leftarrow \min\{D\}$ 
11:    if  $minVal \leq t$  then
12:       $indizes \leftarrow \text{SEARCH}(D, minDist + g)$ 
13:       $S(indizes) \leftarrow 1$ 
14:    end if
15:  end if
16: end for

```

---

## B. Additional Figures

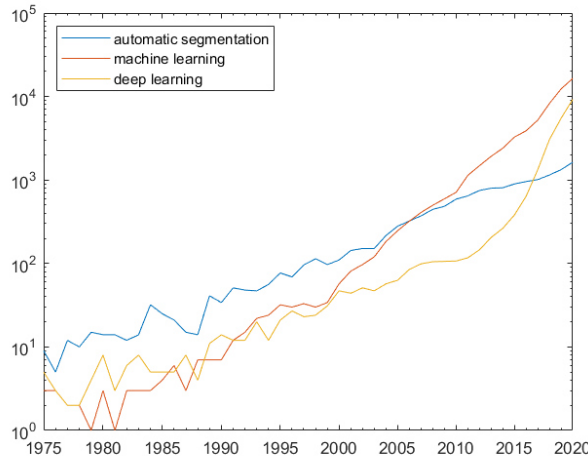


**Figure B.1.:** Number of papers in PubMed<sup>1</sup> for searches on automatic segmentation, machine learning, and deep learning from 1975 to 2020 (logarithmic vertical scale).

---

<sup>1</sup>Data acquired from <https://pubmed.ncbi.nlm.nih.gov/>, accessed 2021-04-10.

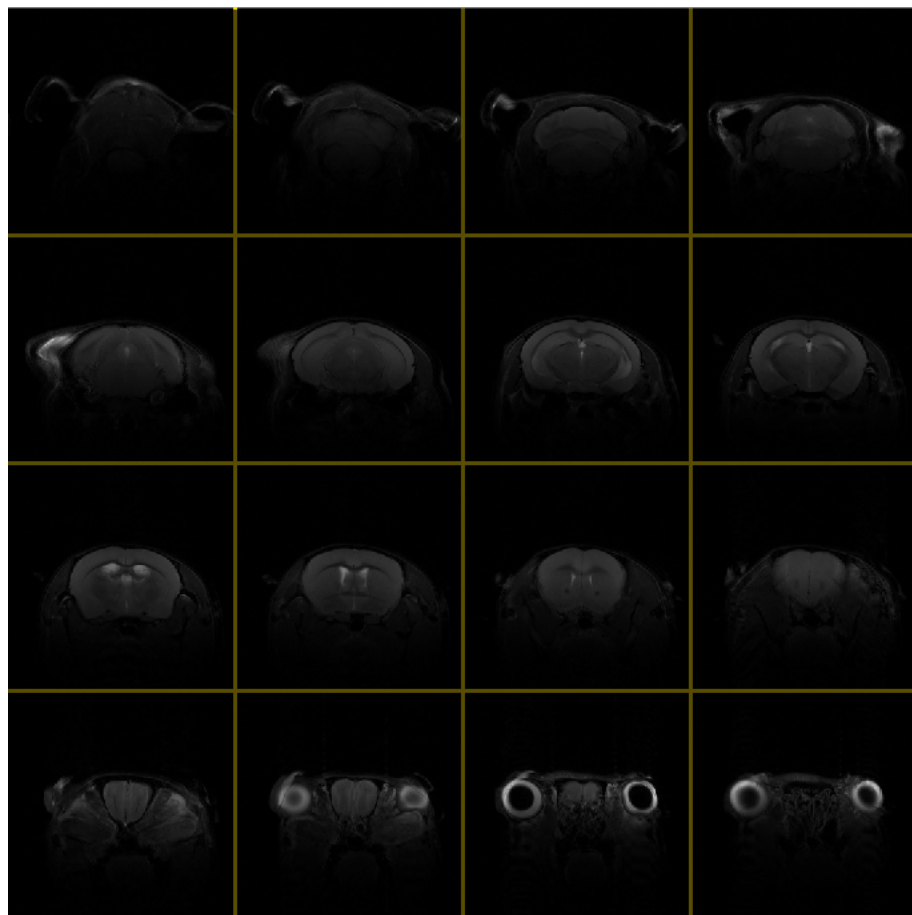


**Figure B.2.:** Representation of sequence 04 (table 3.1), T2 weighted.  
Top to bottom: Slices 1-4 (at Lambda), 5-8, 9-12, 13-16 (between the eyes).

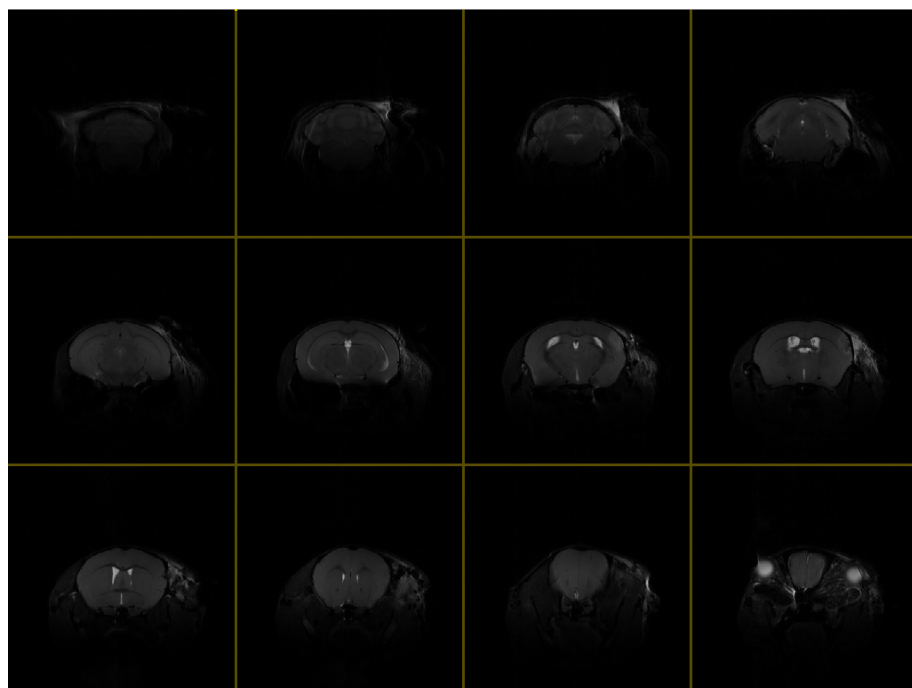
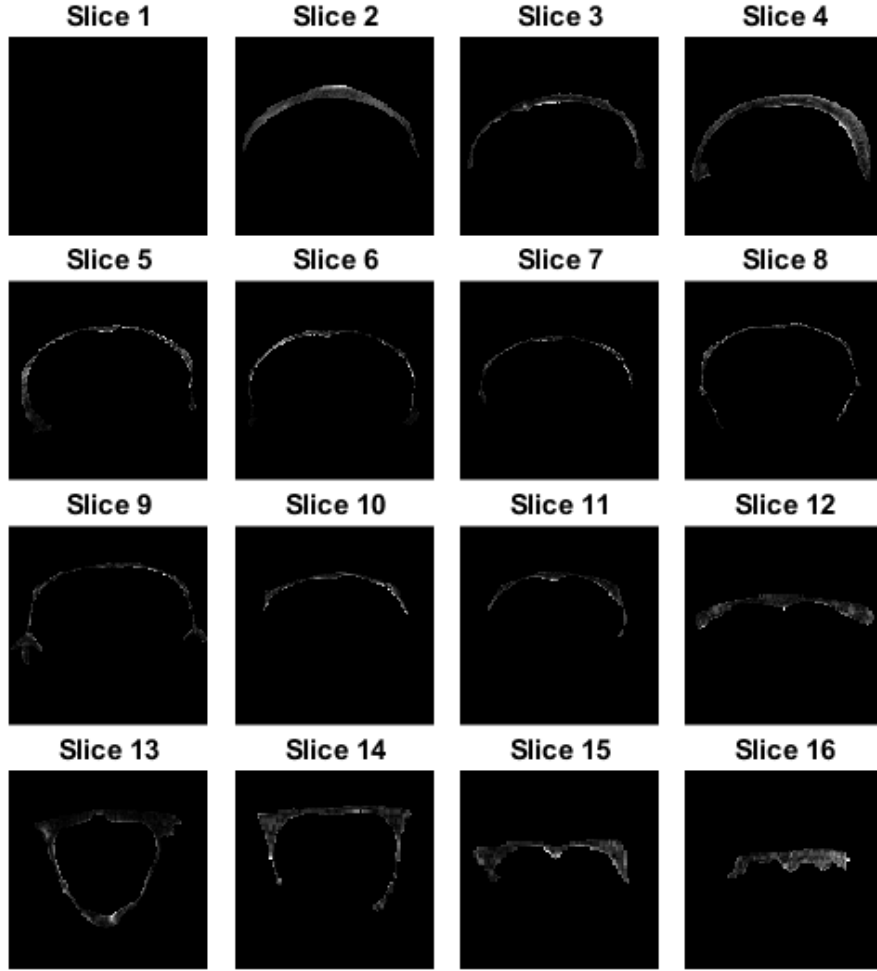
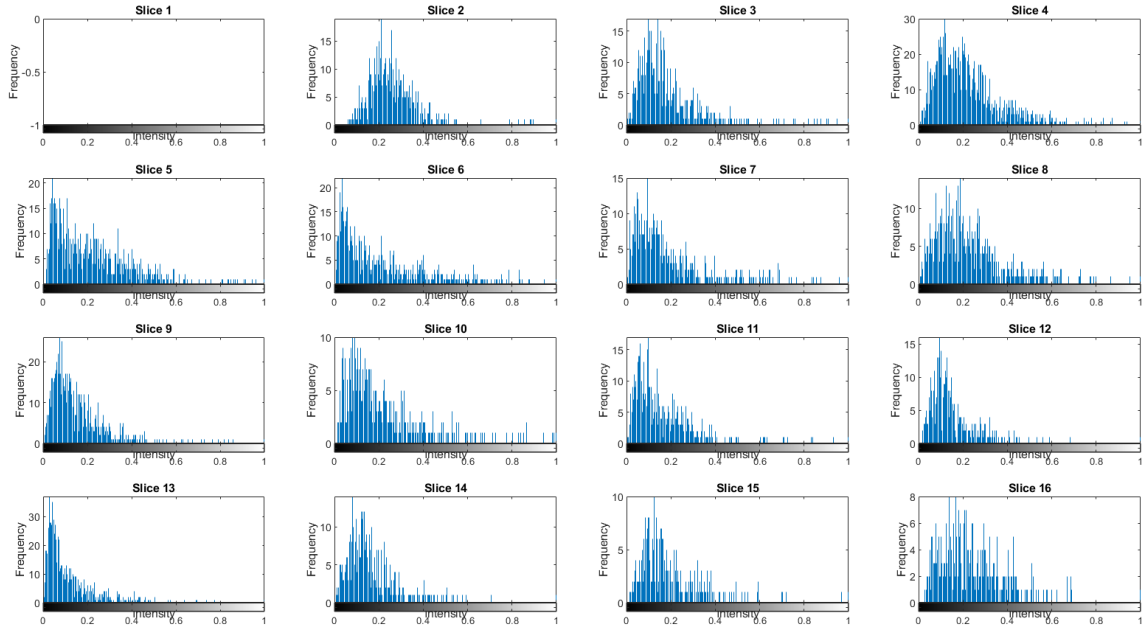


**Figure B.3.:** Representation of sequence ME (table 3.1), T2 weighted.  
Top to bottom: Slices 1-4 (at Lambda), 5-8, 9-12 (between the eyes).

## 5. Appendix



**(a)** Skull segments in slices of sequence 03. In slice 1, the rater did not identify skull tissue.



**(b)** Histograms of the ground truth skull segments in slices of sequence 3. Gray values are normalized to  $[0, 1]$ .

**Figure B.4.:** Skull segments in slices of sequence 03 and their respective histograms according to the ground truth.

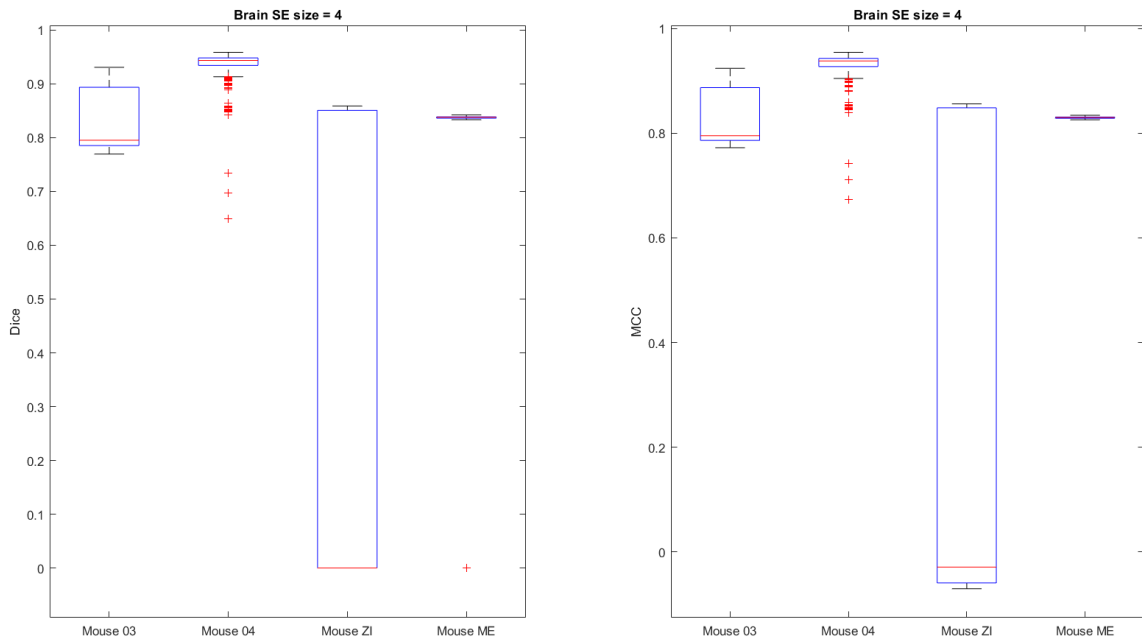


**Figure B.5.:** Evaluation of the brain segmentation for all sequences with  $SE_{Bg} = 4$ .

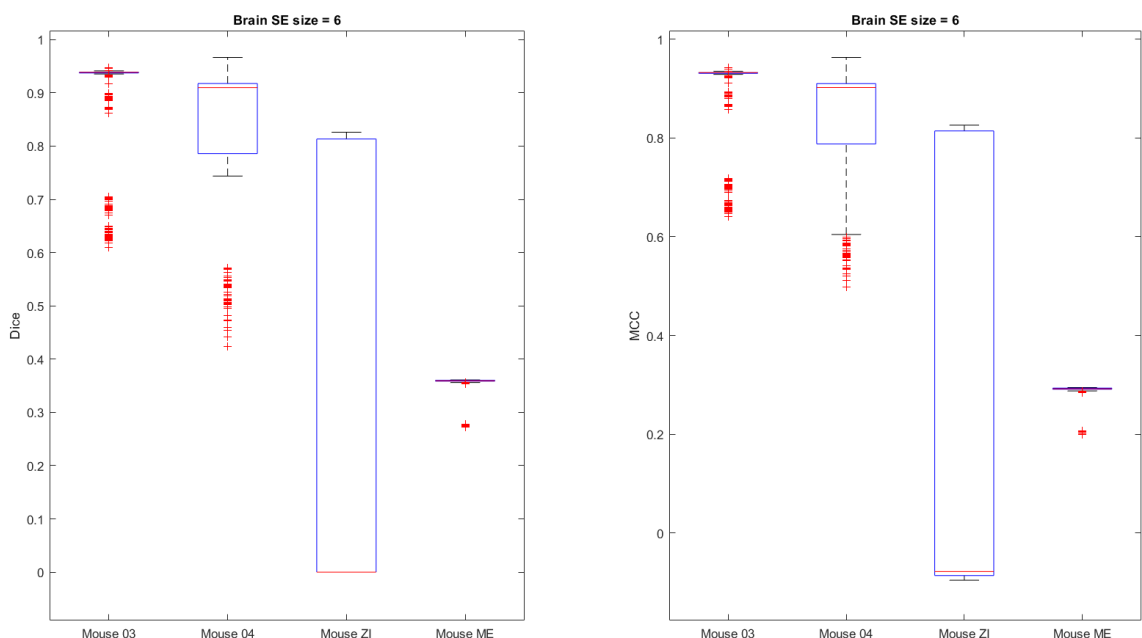


**Figure B.6.:** Evaluation of the brain segmentation for all sequences with  $SE_{Bg} = 6$ .

## 5. Appendix

---

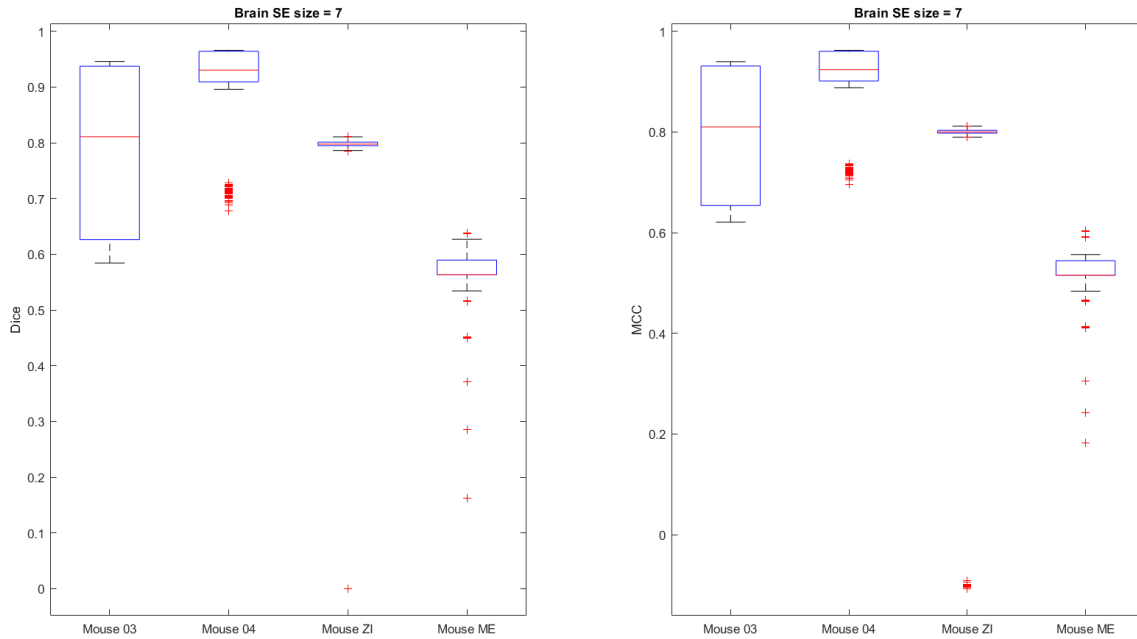


**Figure B.7.:** Evaluation of the brain segmentation for all sequences with  $SE_{Bg} = 7$ .

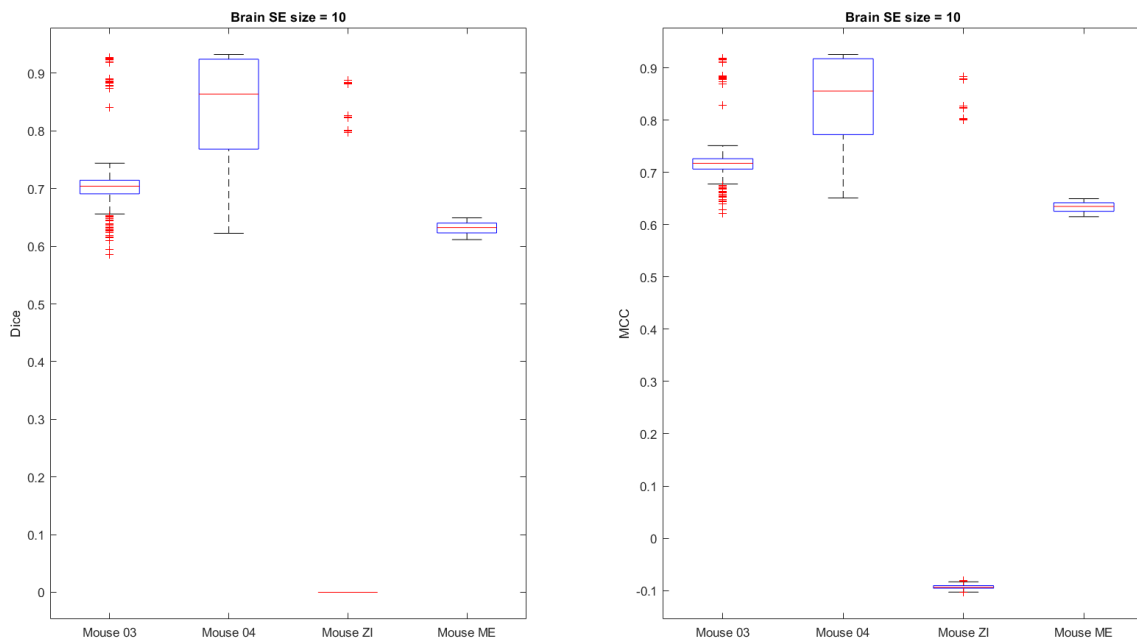
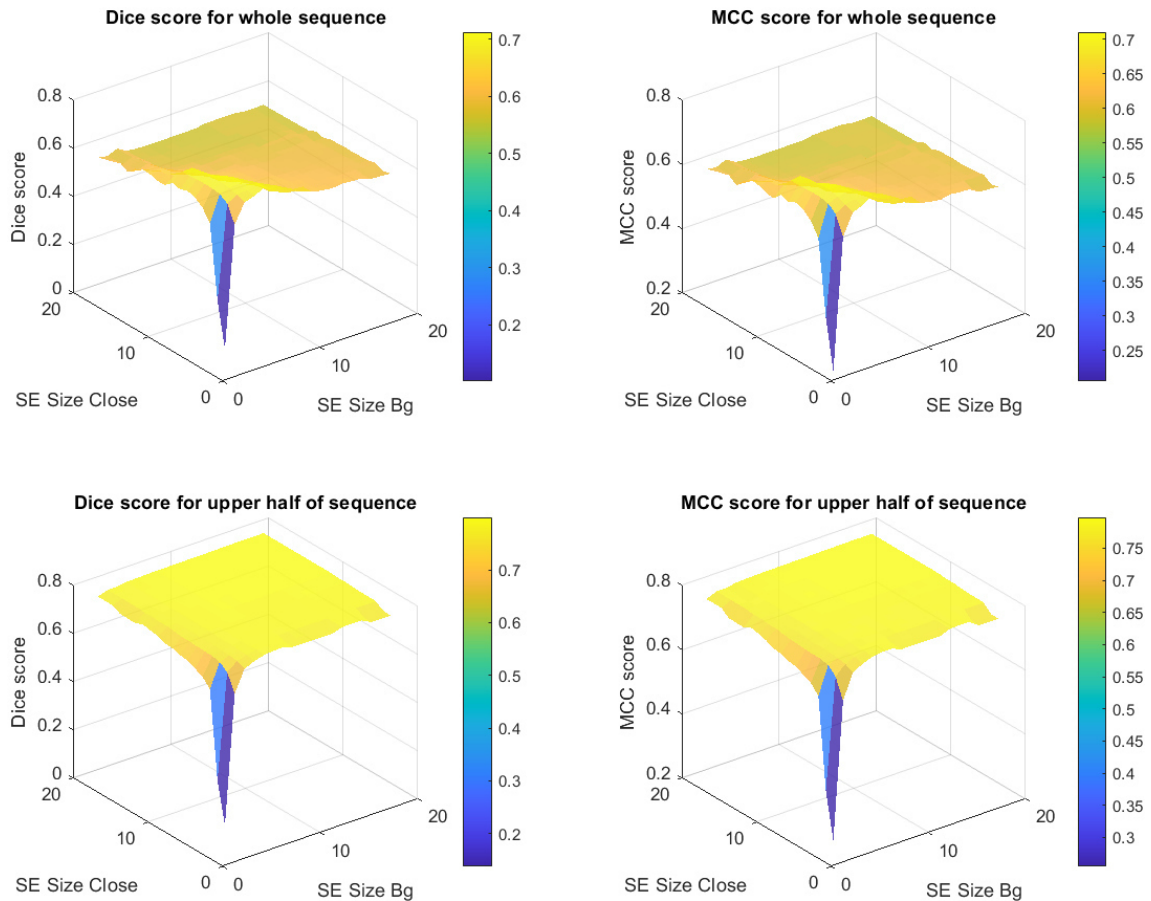
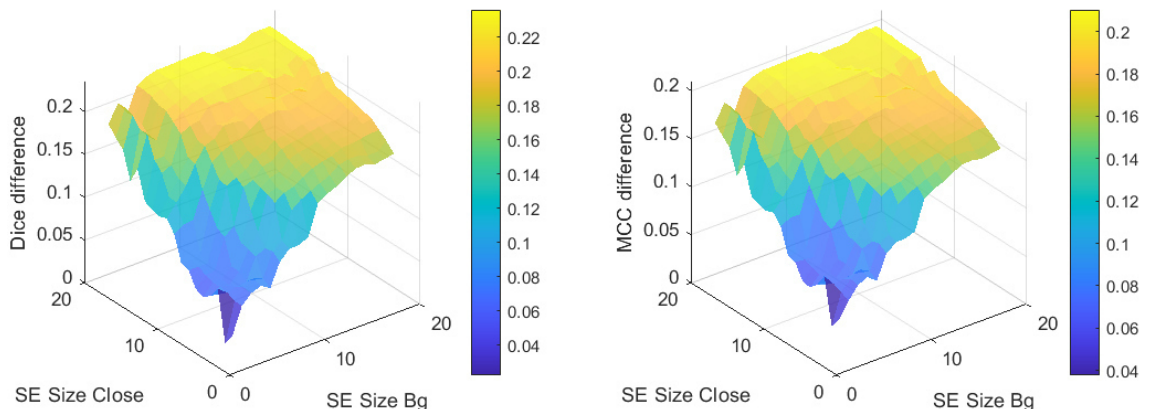


**Figure B.8.:** Evaluation of the brain segmentation for all sequences with  $SE_{Bg} = 10$ .



**(a)** Dice score and MCC score for each pairwise selection of the foreground segmentation parameters. Top row: Scores calculated on the whole the sequence. Bottom row: Scores calculated on the upper half of the sequence.



**(b)** Difference between the scores calculated on the whole sequence and calculated on the upper half of the sequence for each metric.

**Figure B.9.:** Results for the pairwise selection of the foreground segmentation of sequence 04 with brain ground truth as brain segmentation.

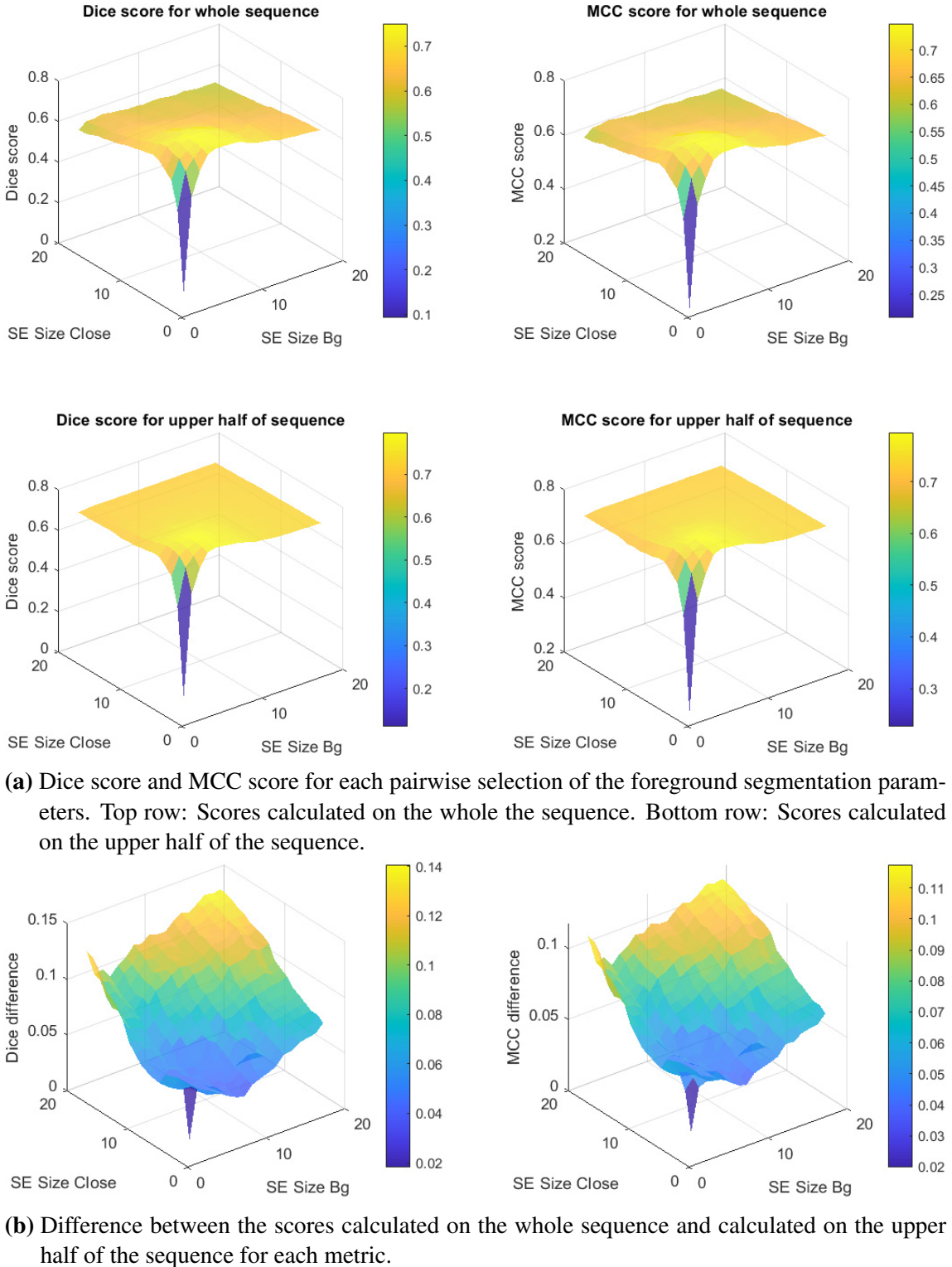
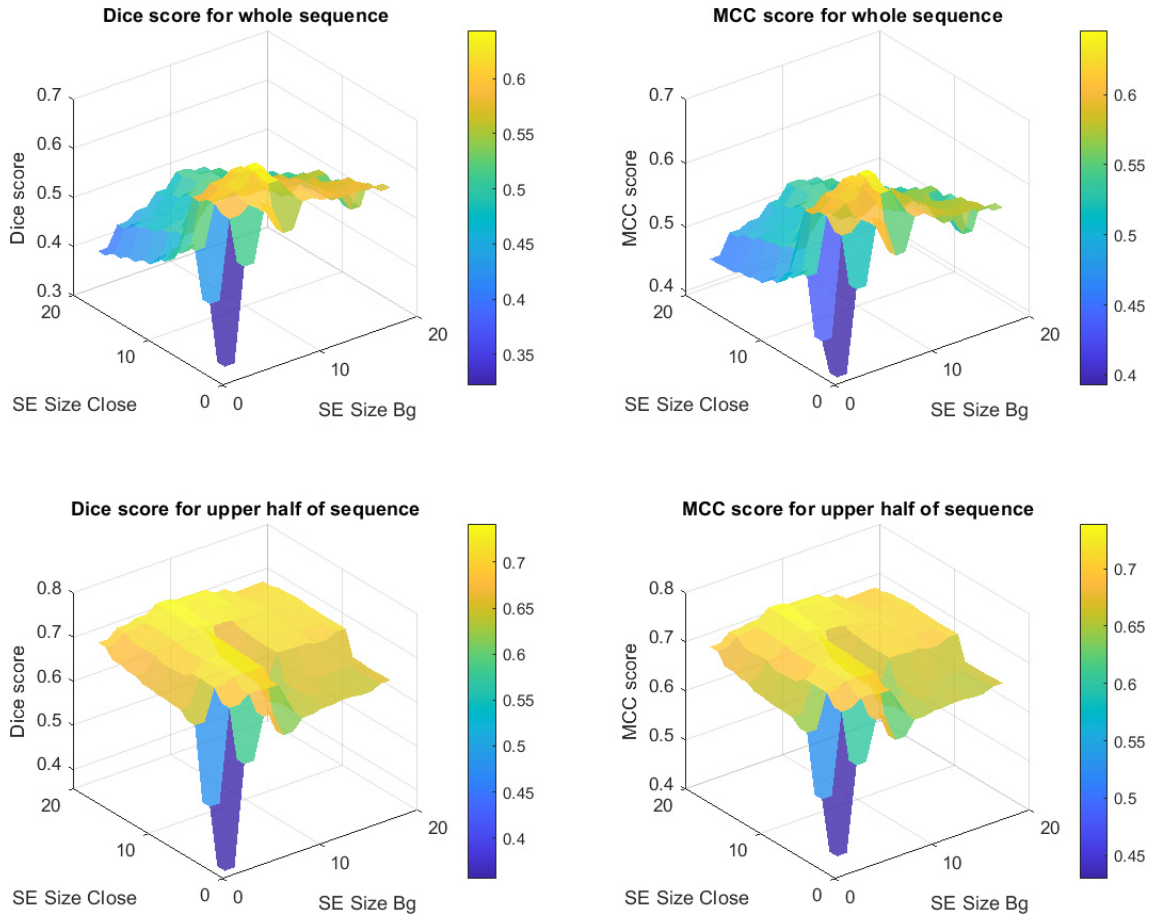
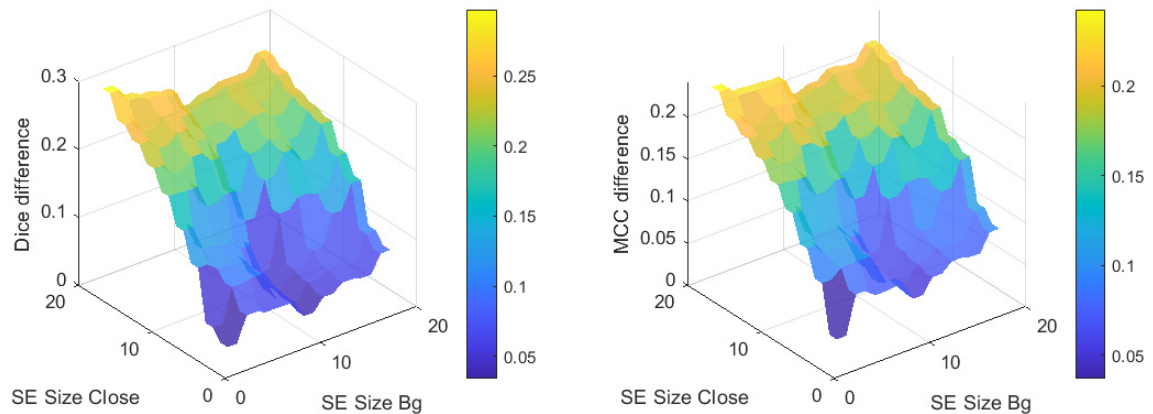


**Figure B.10.:** Results for the pairwise selection of the foreground segmentation of sequence *ZI* with brain ground truth as brain segmentation.



**(a)** Dice score and MCC score for each pairwise selection of the foreground segmentation parameters. Top row: Scores calculated on the whole the sequence. Bottom row: Scores calculated on the upper half of the sequence.



**(b)** Difference between the scores calculated on the whole sequence and calculated on the upper half of the sequence for each metric.

**Figure B.11.:** Results for the pairwise selection of the foreground segmentation of sequence *ME* with brain ground truth as brain segmentation.

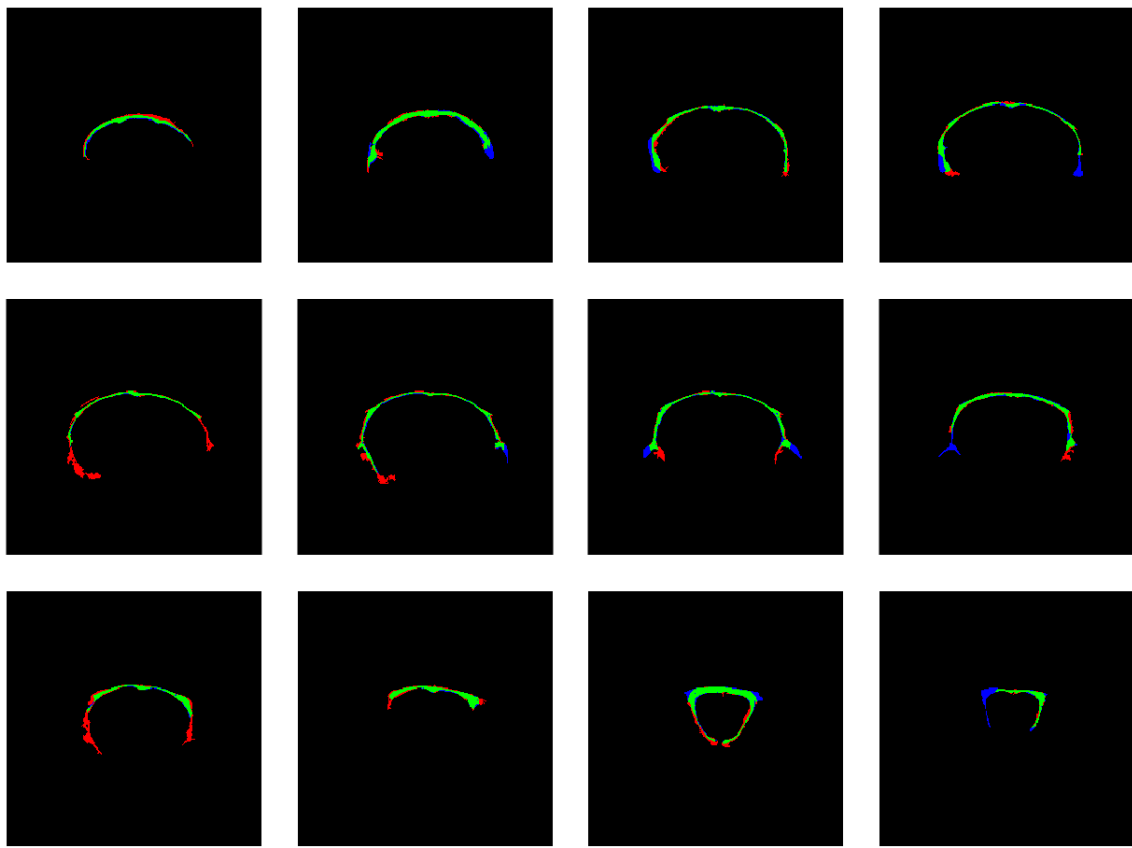


**Figure B.12.:** Exemplary output of the automatic skull segmentation for sequence 04.  
Green: True positives  $TP$ , Red: False positives  $FP$ , Black: True negatives  $TN$ , Blue: False negatives  $FN$ .

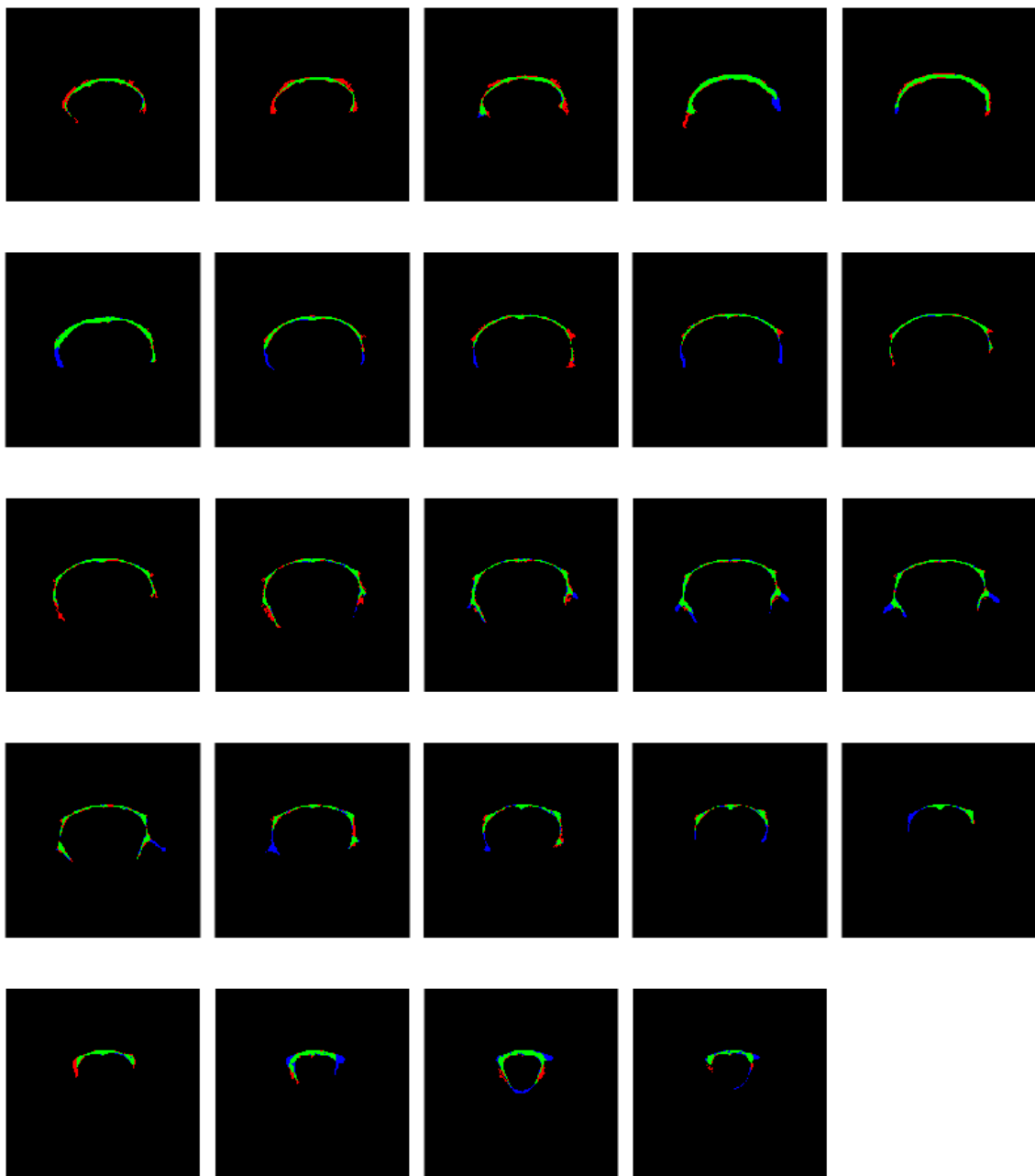


**Figure B.13.:** Exemplary output of the automatic skull segmentation for sequence *ZI*.  
Green: True positives *TP*, Red: False positives *FP*, Black: True negatives *TN*, Blue: False negatives *FN*.

# Glossary

**3D-PCNN** Three-dimensional Pulse-coupled Neural Network. Approach presented by [7] to segment the rodent brain in MRI sequences based on the PCNN algorithm presented by Murugavel and Sullivan [24]. xi, 16–18, 26, 28, 39, 41, 42, 58, 59, 63, 65

**AuSoMS** The method developed in this work (Automatic Segmentation of the Mouse Skull in MRI). 7, 9–11, 13, 15–21, 23, 25, 30, 35, 36, 38, 39, 41, 42, 58, 59

**DICOM** Digital Imaging and Communications in Medicine. Official standard for sharing and storage of medical imaging data [30]. 7, 9, 58, 59

**HEiKA** The Heidelberg Karlsruhe Strategic Partnership. 1, 3, 7, 8, 31, 34, 36, 41, 42, 58, 59

**MATLAB** Commercial software focusing on numerical calculations using matrices. MATLAB version R2020b is used in this thesis for the implementation of the approach. 9–12, 14, 21, 22, 28, 38, 39, 42, 58, 59

**MATLAB File Exchange** Public repository for MATLAB code. <https://de.mathworks.com/matlabcentral/fileexchange/>, accessed 2021-04-16. 9, 58, 59

**MRgFUS** Focused ultrasound used together with magnetic resonance imaging for guidance and monitoring. 1, 58, 59

**U-Net** Implementation of Convolutional Neural Networks. Originally invented for biomedical image classification tasks [31]. 6, 42, 58, 59

# Acronyms

**$\mu$ CT** Micro-computed Tomography. 6, 58, 59

**3D-PCNN** Three-dimensional Pulse-coupled Neural Network Algorithm. 6, 58, 59

**AD** Alzheimer's disease. 1, 58, 59

**AHE** Adaptive Histogram Equalization. 10, 58, 59

**AuSoMS** Automatic Segmentation of the Mouse Skull in MR images. 7, 58, 59

**BBB** blood-brain barrier. 1, 42, 58, 59

**CEM** Classification Expectation Maximization. 6, 58, 59

**CLAHE** Contrast Limited Adaptive Histogram Equalization. 10–12, 41, 58, 59, 63

**CNN** Convolutional Neural Network. 5, 58, 59

**CT** Computed Tomography. 5, 6, 58, 59, 63

**DWI** Diffusion-weighted Imaging. 6, 58, 59

**FUS** Focused Ultrasound. 1–3, 8, 9, 42, 58, 59

**HE** Histogram Equalization. 10, 58, 59

**IAR-IPR** Institute for Anthropomatics and Robotics - Intelligent Process Control and Robotics. 58, 59

**IPE** Institute for Data Processing and Electronics. 1, 58, 59

**KIT** Karlsruhe Institute of Technology. 1, 58, 59

**MCC** Matthews Correlation Coefficient. 26, 28–30, 32–37, 53–55, 58, 59, 63, 64

**MICO** Multiplicative Intrinsic Component Optimization. 16, 39, 58, 59

**MITK** Medical Imaging Interaction Toolkit. 8, 58, 59

**MR** Magnetic Resonance. 1, 3, 5–7, 9, 34, 41, 42, 58, 59, 61, 63

**MRI** Magnetic Resonance Imaging. 1, 2, 4–6, 8, 9, 16, 19, 21, 34–36, 41, 42, 58, 59

**NLMF** Non-local Means Filtering. 12, 39, 41, 58, 59

## *Acronyms*

---

**PCNN** Pulse-coupled Neural Network. 16, 58, 59

**PVE** partial volume effect. 2, 8, 9, 41, 58, 59

**ROI** region of interest. 19, 20, 39, 58, 59

**SE** structural element. 13, 17, 19, 27, 28, 31, 33, 35, 41, 58, 59

**SNR** signal-to-noise ratio. 1, 9, 58, 59

# List of Figures

1.1. Representation of sequence <i>03</i> (table 3.1), T2 weighted . . . . .	2
1.2. Dorsal skull aspect as shown in Cook [8] . . . . .	3
1.3. Slice thickness and spacing between slices . . . . .	3
1.4. Depiction of an optimal skull segmentation . . . . .	4
2.1. Number of papers in PubMed for searches on automatic segmentation of bone in CT (respective MR) images from 1995 to 2020 (linear vertical scale) . . . . .	6
3.1. Measured thickness of the skull in exemplary slices of sequence <i>03</i> using ground truth data . . . . .	8
3.2. Estimated bias field in separate slices of sequence <i>03</i> according to Li et al. [21] . . . . .	9
3.3. Effect of the CLAHE application . . . . .	11
3.4. Visualization of the pre-processing step using 3 exemplary slices . . . . .	12
3.5. Foreground segmentation . . . . .	14
3.6. Foreground segmentation of sequence <i>03</i> . . . . .	15
3.7. Bias field correction . . . . .	16
3.8. Processing flow of 3D-PCNN as shown in [7] . . . . .	17
3.9. Brain mask volume plotted against iteration number as shown in [7] . . . . .	18
3.10. Exemplary brain segmentation . . . . .	18
3.11. Combination of brain segmentation and foreground segmentation. The respective segments are color-coded. Magenta: $\tilde{F}$ . Green: $R$ . White: $F_{roi}$ . . . . .	20
3.12. Illustration: Measurement of the maximum Feret diameter and the minimum Feret diameter . . . . .	21
3.13. Measurements of the maximum feret diameter in pixels of all objects in an exemplary slice of $F_{roi}$ . . . . .	21
3.14. Outlier correction on an exemplary binary mask . . . . .	22
3.15. Exemplary slice in which the skull consists of two segments . . . . .	23
3.16. Close-up view of an exemplary gap between two segments . . . . .	23
4.1. Evaluation of the brain segmentation for all sequences with $SE_{Bg} = 5$ . . . . .	27
4.2. Median scores for the brain segmentation on all 4 sequences for different SE sizes . . . . .	28
4.3. Comparison between a rather good brain segmentation and a worse brain segmentation of the same sequence . . . . .	29
4.4. Evaluation of the brain segmentation for all sequences using the introduced algorithm 1 for variance compensation. . . . .	31
4.5. Results for the pairwise selection of the foreground segmentation of sequence <i>03</i> with brain ground truth as brain segmentation . . . . .	32
4.6. Pairwise correlation coefficients for the different MCC score matrices of all sequences. . . . .	34
4.7. Pairwise correlation coefficients for $\tilde{W}$ , $\tilde{U}$ , and $\tilde{A}$ . . . . .	35

4.8. Exemplary output of the automatic skull segmentation for sequence <i>03</i> . Green: True positives <i>TP</i> , Red: False positives <i>FP</i> , Black: True negatives <i>TN</i> , Blue: False negatives <i>FN</i> . . . . .	36
4.9. Median scores for brain segmentation, skull segmentation on the whole sequence, and segmentation of the skullcap . . . . .	37
4.10. Dice score and MCC score for the brain segmentation of all 4 sequences and 1000 repetitions per sequence . . . . .	37
4.11. Results for the skull segmentation on whole sequence of all 4 sequences and 1000 repetitions per sequence . . . . .	38
4.12. Results for the skull segmentation on the upper half of all 4 sequences and 1000 repetitions per sequence . . . . .	38
B.1. Number of papers in PubMed for searches on automatic segmentation, machine learning, and deep learning from 1975 to 2020 (logarithmic vertical scale) . . . . .	48
B.2. Representation of sequence <i>04</i> (table 3.1), T2 weighted . . . . .	49
B.3. Representation of sequence <i>ME</i> (table 3.1), T2 weighted . . . . .	49
B.4. Skull segments in slices of sequence <i>03</i> and their respective histograms according to the ground truth . . . . .	50
B.5. Evaluation of the brain segmentation for all sequences with $SE_{Bg} = 4$ . . . . .	51
B.6. Evaluation of the brain segmentation for all sequences with $SE_{Bg} = 6$ . . . . .	51
B.7. Evaluation of the brain segmentation for all sequences with $SE_{Bg} = 7$ . . . . .	52
B.8. Evaluation of the brain segmentation for all sequences with $SE_{Bg} = 10$ . . . . .	52
B.9. Results for the pairwise selection of the foreground segmentation of sequence <i>04</i> with brain ground truth as brain segmentation . . . . .	53
B.10. Results for the pairwise selection of the foreground segmentation of sequence <i>ZI</i> with brain ground truth as brain segmentation . . . . .	54
B.11. Results for the pairwise selection of the foreground segmentation of sequence <i>ME</i> with brain ground truth as brain segmentation . . . . .	55
B.12. Exemplary output of the automatic skull segmentation for sequence <i>04</i> . Green: True positives <i>TP</i> , Red: False positives <i>FP</i> , Black: True negatives <i>TN</i> , Blue: False negatives <i>FN</i> . . . . .	56
B.13. Exemplary output of the automatic skull segmentation for sequence <i>ZI</i> . Green: True positives <i>TP</i> , Red: False positives <i>FP</i> , Black: True negatives <i>TN</i> , Blue: False negatives <i>FN</i> . . . . .	57

# List of Tables

3.1. DICOM sequences . . . . .	7
4.1. Exemplary segmentation computation times using a single 3D-PCNN brain segmentation. . . . .	39
4.2. Exemplary computation times of pre-processing and bias field correction. . . . .	39

# List of Algorithms

1.	Variance compensation . . . . .	30
2.	Outlier correction . . . . .	47
3.	Post-processing . . . . .	48

## BibTex Entry of this Thesis

```
@mastersthesis{Luca Springer_03. May 2021,  
  author = {Luca Springer},  
  editor = {M. Sc. Paul Scheikl},  
  ipr-thesis = Bachelor Thesis,  
  keywords = {automatic segmentation, mouse, rodent, skull, brain, MRI, FUS, MRgFUS},  
  location = {Karlsruhe, Germany},  
  month = ,  
  pages = ,  
  school = {Karlsruhe Institute of Technology},  
  title = {Automatic Segmentation of the Mouse Skull in MR Images for MRI Guided  
Focused Ultrasound Therapy},  
  year = {03. May 2021}  
}
```